Anodic Oxidation Enabled Cation Leaching for Promoting Surface Reconstruction in Water Oxidation

Yan Duan,[Δ][a][b] Jun Yan Lee,[Δ][a] Shibo Xi,[c] Yuanmiao Sun,[a] Jingjie Ge,[a] Samuel Jun Hoong Ong,[a][d] Yubo Chen,[a][e] Shuo Dou,[f] Fanxu Meng,[a][d] Caozheng Diao,[c] Adrian C. Fisher,[e][g] Xin Wang,[f] Günther G. Scherer,[h][i] Alexis Grimaud,*[j][k] Zhichuan J. Xu*[a][b][d][e]

[a] Y. Duan, J. Y. Lee, Dr. Y. Sun, Dr. J. Ge, S. J. H. Ong, Dr. Y. Chen, F. Meng, and Dr. Z. Xu
School of Materials Science and Engineering
Nanyang Technological University
50 Nanyang Avenue, Singapore 639798, Singapore
E-mail: xuzc@ntu.edu.sg (Z. Xu)

[b] Y. Duan and Dr. Z. Xu
Energy Research Institute @ NTU, ERI@N, Interdisciplinary Graduate School
Nanyang Technological University
50 Nanyang Avenue, Singapore 639798, Singapore

[c] Dr. S. Xi and Dr. C. Diao
Institute of Chemical and Engineering Sciences
Agency for Science, Technology and Research (A*STAR)
1 Pesek Road, Singapore 627833, Singapore

[d] S. J. H. Ong, F. Meng, and Dr. Z. Xu
Singapore-HUJ Alliance for Research and Enterprise, NEW-CREATE Phase II
Campus for Research Excellence and Technological Enterprise (CREATE)
1 CREATE Way, Singapore 138602, Singapore

[e] Dr. Y. Chen and Dr. Z. Xu
The Cambridge Centre for Advanced Research and Education in Singapore
1 CREATE Way, Singapore 138602, Singapore

[f] Dr. S. Dou and Dr. X. Wang
School of Chemical and Biomedical Engineering
Nanyang Technological University
62 Nanyang Drive, Singapore 637459, Singapore

[g] Dr. A. C. Fisher
Department of Chemical Engineering
University of Cambridge
Cambridge, CB2 3RA United Kingdom

[h] Dr. G. G. Scherer
Informetrics Research Group
Ton Duc Thang University
Ho Chi Minh City, Vietnam

[i] Dr. G. G. Scherer
Faculty of Applied Sciences
Ton Duc Thang University
Ho Chi Minh City, Vietnam

[j] Dr. A. Grimaud
Chimie du Solide et de l'Energie
Collège de France
UMR 8260, 75231 Cedex 05 Paris, France
Email: alexis.grimaud@college-de-france.fr (A.Grimaud)

[k] Dr. A. Grimaud
Réseau sur le Stockage Electrochimique de l'Energie (RS2E)
CNRS FR3459
80039 Cedex Amiens, France

Δ These authors contributed equally

Supporting information for this article is given via a link at the end of the document.

Abstract: A rational design on oxygen evolution reaction (OER) catalysts is pivotal to the overall efficiency of water electrolysis. Numerous works have been devoted to understanding the cation leaching and surface reconstruction of some very active electrocatalysts, while few have been on intentionally promoting the surface in a controlled fashion. In this work, we report controllable anodic leaching of Cr in $CoCr_2O_4$ by activating the pristine material at high potential, which enables the transformation of inactive spinel $CoCr_2O_4$ into a highly active catalyst. The depletion of Cr and consumption of lattice oxygen facilitate surface defects and oxygen vacancies, exposing Co species to reconstruct into active Co oxyhydroxides differ from CoOOH. A novel mechanism with the evolution of tetrahedrally coordinated surface cation into octahedral configuration via non-concerted proton-electron transfer is proposed. This work shows the importance of controlled anodic potential in modifying the surface chemistry of electrocatalysts.

Introduction

The ever-increasing consumption of fossil fuels has raised environmental concerns to an alarming point, while not fulfilling the global demand for energy which is continuously growing. This calls for the use of clean energy carriers, among which hydrogen is foreseen as a fuel of great interest for numerous industrial and chemical applications. While so-far largely produced (> 95%) by fossil-fuel reforming, hydrogen can be sustainably produced from water electrolysis, the efficiency of which is limited by the kinetics of the oxygen evolution reaction (OER) at the anode.[1,2] To improve the sluggish reaction kinetics of OER, hence the overall efficiency for hydrogen production, recent research focuses on the development of earth-abundant transition metal oxides/(oxy)hydroxides as electrocatalysts showing promising performances in alkaline conditions.[2–9]

A rational design of catalysts can be guided by understanding their structural/elemental properties which determine the reaction mechanism and activity. Following pioneering work performed on the dimensionally stable anode (DSA) in the 70s[10] and 80s[11,12], from 2011 onwards, several novel activity descriptors have been developed,[2,13–20] such as electron occupancy, covalency, structure and exchange interaction for transition metal oxides which can be related to M−O binding energy. While several research works have reported the surface reconstruction for some very active materials,[21–28] it remains yet almost impossible to predict the activity of these materials based on their M−O binding energy as a consequence of the constantly evolving surface during OER.[29–31] For instance, the surface of $Ba_{0.5}Sr_{0.5}Co_{0.8}Fe_{0.2}O_{3-\delta}$ (BSCF)[22,32,33] rapidly evolves into an amorphous oxyhydroxide after few cycles under OER conditions, this process is accompanied by the leaching of soluble Ba^{2+} and Sr^{2+} ions, and the dissolution and redeposition of Co^{3+} and Fe^{3+} transition metal cations[22]. Furthermore, the Sr^{2+} substitution in $La_{1-x}Sr_xCoO_{3-\delta}$ (LSC)[23] triggers the formation of electrophilic oxygen species "O^{n-}" by decreasing the Fermi level energy into oxygen bands and induces a lattice oxygen participation mechanism. Several works[34–36] have shown that such lattice oxygen involvement leads to surface instabilities for LSC at large Sr^{2+} substitution level. In other catalyst systems with soluble cations, such as $CoFe_xAl_{2-x}O_4$[24] in alkaline solutions and $SrCo_{0.9}Ir_{0.1}O_{3-\delta}$[28], Sr_2FeIrO_6[27] and $Sr_2Fe_{0.5}Ir_{0.5}O_4$[27] in acidic solutions, the leaching of cations leads to further reconstruction of surface species, which results in outstanding OER activity.

However, efforts aiming at the design of catalysts with controllable cation leaching and surface reconstruction towards a highly active surface for OER remain limited[38]. Here, we report controllable leaching of Cr from $CoCr_2O_4$ spinel oxide to promote surface reconstruction for boosting its OER activity. By activating $CoCr_2O_4$ at high potential, Cr leaching occurs and leads to the reconstruction of Co species into oxyhydroxide. The leaching increases with the applied anodic potential and is facilitated by the activation of lattice oxygen redox which gives rise to favourable surface condition for vigorous reorganization and activity enhancement. $CoCr_2O_4$ activated at 1.7 V for 1.5 hours (Act-$CoCr_2O_4$) exhibits one magnitude higher performance than pristine $CoCr_2O_4$ (Pri-$CoCr_2O_4$), which outperforms CoOOH thin film. The surface electronic structure and surface-active sites for Act-$CoCr_2O_4$ have been probed in comparison to CoOOH and NiFeOOH-Cr. This facilitates the understandings of the role Cr leaching plays in Act-$CoCr_2O_4$. Our work demonstrates a promising way to achieve controllable electrochemical reconstruction for transition metal spinel oxides. It broadens our understandings of surface evolution of spinel oxides during OER and enlightens that tunable design of highly active OER catalysts is achievable. Furthermore, it enlightens the surface regulation and activity promotion of other catalysts with soluble cations in the structure.

Results and Discussion

Crystal structure characterization. The $CoCr_2O_4$ oxide was synthesized via a sol–gel method. The crystal structures of $CoCr_2O_4$ were characterized by powder X-ray diffraction (XRD). As displayed in Figure 1a, the diffraction peaks of the as-prepared $CoCr_2O_4$ match with that of the standard cubic spinel (*Fd*-3*m*) oxides. The XRD pattern of $CoCr_2O_4$ exhibits a shift to lower angles when compared to Co_3O_4. This shift is ascribed to an increase in the lattice parameter with Cr substitution. As determined by X-ray absorption near edge structure (XANES) spectroscopies, Co and Cr in $CoCr_2O_4$ possess an oxidation state of Co^{2+} and Cr^{3+}, respectively (left panel in Figure 1b and Figure 1c). A sharp Co K pre-edge (inset of the left panel in Figure 1b) represents a transition from 1*s* to 3*d* with a strong 3*d* - 4*p* orbitals mixing at non-centrosymmetric sites[40], indicating the tetrahedral occupation[14] of Co^{2+}. This site occupation has been further confirmed with extended X-ray absorption fine structure (EXAFS). The second Fourier transform peaks reveal the distances between the absorbing metal atoms and their neighbouring atoms in either the octahedral site or tetrahedral site. The distances between Co atoms and their neighbouring metal cations which occupy octahedral sites are around 3.0 Å, indicating the Co atoms accommodating the centre of tetrahedrons[41] (right panel in Figure 1b). Cr atoms have 2.5 Å distance away from their neighbouring metal atoms, suggesting that Cr prefers to stay in octahedral sites of $CoCr_2O_4$[41] (right panel in Figure 1c).

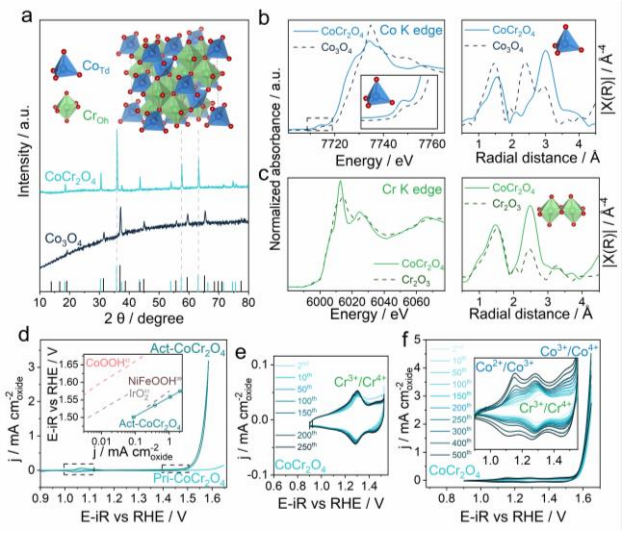

Figure 1. Crystal structure of $CoCr_2O_4$ and OER activity of Pri-$CoCr_2O_4$ and Act-$CoCr_2O_4$. (a) Powder XRD patterns of the as-synthesized $CoCr_2O_4$ and Co_3O_4. The crystal structure of $CoCr_2O_4$ in spinel structure (AB_2O_4) is shown in the inset. Co_{Td} and Cr_{Oh} are tetrahedrally and octahedrally coordinated transition metal cations, respectively. (b) Left panel, normalized Co K-edge XANES spectra for $CoCr_2O_4$. Co_3O_4 is used as a reference. Inset is the pre-edge features of Co K-edge XANES. Right panel, Fourier transform of the EXAFS (FT-EXAFS) for Co K-edge. The second and third peak ≈2.5 Å (TM_{Oh}–TM_{Oh}) and at ≈3.0 Å (i.e. TM_{Td}–TM_{Td} or TM_{Td}–TM_{Oh}) are interatomic metal–metal distances from the absorbing metal atom Co to the second nearest neighbor metal atoms at the octahedral or tetrahedral site. (c) Normalized Cr K-edge XANES spectra (left panel) and FT-EXAFS for Cr K-edge (right panel). (d) Electrochemical characterization of OER performance of $CoCr_2O_4$. CV curves of $CoCr_2O_4$ at the 2nd cycle and after Chronoamperometry (CA) at a potential of 1.7V for 1.5 hours. Inset shows the Tafel plot for surface-area-normalized $CoCr_2O_4$ after CA at a potential of 1.7 V for 1.5 hours compared with IrO_2[42]. All data points and error bars were obtained by averaging the results of at least three independent measurements. (e) CV cycling of $CoCr_2O_4$ at the low potential range prior to OER from 0.9 V to 1.52 V. (f) CV cycling of $CoCr_2O_4$ in 1M KOH at 10 mV s^{-1} from 0.9 V to 1.66 V. Inset shows the evolutive redox peaks for $CoCr_2O_4$ 2nd to 500th cycle CV in between 0.904 and 1.624 V.

Electrochemical study. Electrochemical measurements were then performed using the $CoCr_2O_4$ catalyst. Activities normalized by the BET surface area for the pristine material (Pri-$CoCr_2O_4$) (Table S1, Supporting Information), are presented in Figure 1d. There, the Pri-$CoCr_2O_4$ catalyst shows limited activity in 1 M KOH. Chronoamperometry (CA) measurements were conducted on $CoCr_2O_4$ by holding the electrode at different potentials, varying from 1.5, 1.6, 1.64 to 1.7 V (all potentials are quoted in the reversible hydrogen electrode (RHE) scale), for 7 hours total. Faster stabilization for the current density at higher value is observed when applying greater potentials (Supporting Information Figure S1). Longer time for the activation by CA at lower potential does not increase the stabilized current density further (Supporting Information Figure S2 and Figure S3). Besides, continuous CV cycles after CA at lower potential does not give rise to the same activity as activated at high potential. (Supporting Information Figure S4). This potential dependent activity is presented in the Tafel plots in Supporting Information Figure S5. It is confirmed by the decreased charge transfer resistance at higher potential as observed by Electrochemical Impedance Spectroscopy (EIS) as shown in Supporting Information Figure S6. After activation at a potential of 1.7 V for 1.5 hours in 1 M KOH (Act-$CoCr_2O_4$), the current becomes stable (Supporting Information Figure S1). The current density for Act-$CoCr_2O_4$ increases more than one magnitude and becomes superior to that of IrO_2[42] (inset of Figure 1d). By normalising the activity by electrochemical active surface area (ECSA), (Supporting Information Figure S7, S8, S9) the intrinsic activity for Act-$CoCr_2O_4$ exceeds that of CoOOH[43] (Supporting Information Figure S10). This increase in activity by activation is not attributed to the chemical reaction. Indeed, after soaking the $CoCr_2O_4$ electrode in KOH for 5 hours (Supporting Information Figure S11), the activity is not promoted at all. Besides, the possibility of the activity enhancement from the Fe contamination is excluded by using further purified KOH for the OER measurements. Details are shown in the experimental sections. As shown in the Supporting Information Figure S12, the Tafel slopes remain ~60 mV dec^{-1} by activating the electrode after soaking in the KOH solution for 5 hours. This confirms no Fe effect on the $CoCr_2O_4$ electrode. Instead, the effect from activation manifests in the increased electrochemical activity of cobalt surface species which as seen by the redox peaks at 1.1 V and 1.45 V characteristics of the Co^{2+}/Co^{3+} and Co^{3+}/Co^{4+} redox couples, respectively (Supporting Information Figure S13).[33,44–46] This increase in electrochemical active sites of cobalt is not observed when activating $CoCr_2O_4$ at lower potentials, i.e. below 1.5 V (Supporting Information Figure S13). Hence, cycling the pristine catalyst within a voltage range of 0.9 to 1.55 V vs. RHE, prior to OER potential, does not result in the formation of these Co redox peaks (Figure 1e). The surface redox reaction is instead dominated by Cr species, with characteristic redox peaks from Cr^{4+}/Cr^{3+} redox couple observed at 1.3 V (Figure 1e and Supporting Information Figure S14). When the catalyst is subjected to a series of voltammetry cycles from 0.9 to 1.65V, the surface redox activity is initially dominated by the redox reaction of Cr as well (Figure 1f and Supporting Information Figure S14). Along with cycles, two new redox peaks indicative of the activity of the Co^{2+}/Co^{3+} and Co^{3+}/Co^{4+} couples, as seen at ar. 1.1 V and 1.45 V vs. RHE, appear and gradually increase. Thus, the exposure of Co-rich electrochemical active sites to the alkaline electrolyte only occurs for $CoCr_2O_4$ after activation at a higher anodic potential. A series of CA at different potentials followed by one cycle of CV were then conducted for Pri-$CoCr_2O_4$. At a potential of around 1.56 V, there is the formation of Co redox peaks (Figure 2a and Supporting Information Figure S14). This is supported by the Tafel plot extracted from the CV conducted after CA (Supporting Information Figure S5). The obviously decreased Tafel slope (after CA is held at potentials higher than 1.6 V) indicates the change in the reaction path. Besides, as the potential for CA measurement increases to 1.56 V, the current density measured at each potential starts to increase rapidly with time (Supporting Information Figure S15). This observation differs from the one measured for Co_3O_4 which experiences a steady current density at every potential step (Supporting Information Figure S17). Hence, while reaching a certain anodic potential (1.56 V), Co species in $CoCr_2O_4$ starts to contribute to the OER. Besides, the higher the applied anodic potential reached, the better the OER activity manifested. The largely increased electrochemical active surface area (ECSA) for Act-$CoCr_2O_4$ compared to Pri-$CoCr_2O_4$ indicates the increase in number of active sites after activation

(Supporting Information Figure S7 and Figure S8). The current density normalized by ECSA for Act-$CoCr_2O_4$ is still higher than that for Pri-$CoCr_2O_4$, indicates that not only the number of active sites but also the intrinsic activity per site increases after activation (Supporting Information Figure S9).

Surface Composition Characterization. As observed by electrochemical studies, the surface redox activity for Cr cations is dominant at low potentials, while their contribution to the OER activity is minimal. Thus, Co cations dominate the surface reaction at higher potentials and contribute to the enhanced OER activity. To investigate this potentially regulated surface composition, a series of characterizations have been adopted. Inductively coupled plasma mass spectrometry (ICP-MS) was used to test the electrolytes after consecutive series of CA with an interval of 20 minutes at each potential step for $CoCr_2O_4$. In doing so, almost no leaching of Co cations was observed in the electrolyte at the different activation potentials. However, the case is different for Cr. The cumulative mass of Cr leached is initially higher than that of Co and is accelerated after potentiostatic holding at 1.56 V vs. RHE (Figure 2b). The higher the potential at which the $CoCr_2O_4$ is activated, the more Cr is leached out into the solution. Combined with the analysis of current densities under CA in Figure 2a, the occurrence and acceleration of Cr leaching synchronize with the OER activity. Hence, high-resolution transmission electron microscopy (HRTEM) reveals that the surface of Act-$CoCr_2O_4$ is forming an amorphous oxyhydroxide layer with a thickness of more than 5nm (Figure 2c and Figure 2f). To reveal the elemental composition for the surface layer of $CoCr_2O_4$ after activation, scanning transmission electron microscopy energy-dispersive X-ray spectroscopy (STEM-EDS) and line scan were conducted. The Co and Cr species are initially present in the stoichiometric proportion (1:2) on the surface of Pri-$CoCr_2O_4$, as shown in Figure 2d and Supporting Information Figure S18. When subjected to a higher OER potential, the surface profile of Act-$CoCr_2O_4$ shows a significant depletion of Cr and the abundance of Co cations (Figure 2g, Supporting Information Figure S19 and Figure S20). Such observation depicts well the process of Cr leaching and the gradual exposure of Co on the surface of the catalyst under increased applied potential (Figure 2e and 2h). This conclusion is supported by the observation via EXAFS that the local atomic structure changes for $CoCr_2O_4$ before and after the CA step. After CA at the potentials of 1.6 V and 1.64 V vs. RHE, the higher the potential at which $CoCr_2O_4$ is activated, the lower the intensity for Cr-M_{Oh} is found (Supporting Information Figure S21), indicating more Cr leaching. Linking the observations on the change in surface elements with the electrochemical behaviours, the potential at which $CoCr_2O_4$ is activated controls the surface composition and hence the OER activity.

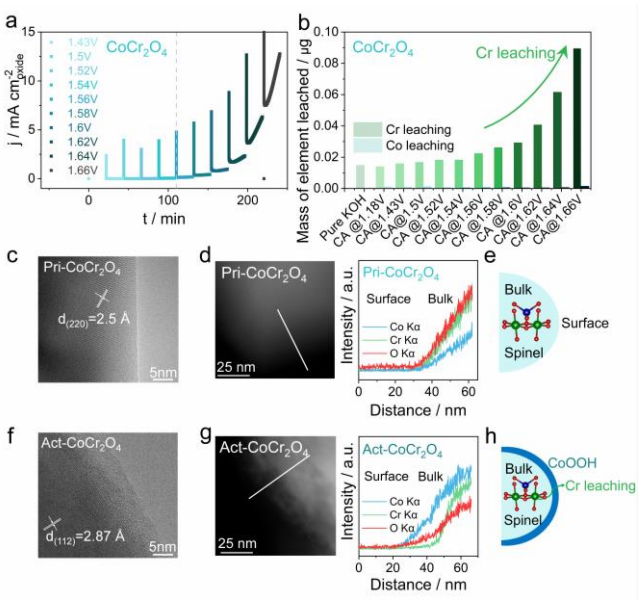

Figure 2. Analysis of surface Cr leaching and reconstruction for Act-$CoCr_2O_4$. (a) A consecutive series of CA at a different potential from 1.43 to 1.66 V for $CoCr_2O_4$. (b) The cumulative mass of element leached after consecutive series of CA conducted at 20mins interval for $CoCr_2O_4$. (c) HRTEM image of Pri-$CoCr_2O_4$. (d) STEM-EDS image and analysis for Pri-$CoCr_2O_4$. (e) Schematic of bulk and surface for Pri-$CoCr_2O_4$. (f) HRTEM image of Act-$CoCr_2O_4$. (g) STEM-EDS image and analysis for Act-$CoCr_2O_4$. (h) Schematic of Cr leaching along with the formation of oxyhydroxide on the surface for Act-$CoCr_2O_4$.

Surface Active Species Characterization. XANES measurements with transmission mode were then conducted before and after CA to reveal the effect of activation potential on the oxidation states and atomic structure of $CoCr_2O_4$. After CA at 1.5 V for 7 hours, the average oxidation state of Co almost does not change. The position of the Co K-edge in $CoCr_2O_4$ is found to shift towards greater energies after activation at 1.6 V or 1.64 V for 7 hours, indicating an increase in the average oxidation state of Co in $CoCr_2O_4$ (Figure 3a and Supporting Information Figure S22). The higher the potential, the higher the oxidation state of Co is presented. The coordination environment of Co in $CoCr_2O_4$ was further investigated by extracting the Co K-edge EXAFS spectra. After CA at potentials higher than 1.6 V, the intensity for the peaks ascribed to Co-O and Co-M_{Oh} (metal cation occupied octahedral site) at around 1.5 Å and 2.5 Å increases along with potential (Figure 3b). This effect may correspond to the increase in the number of Co-O bonds[47,48] and edge shared CoO_6 octahedra. This is accompanied by a decrease in the peak intensity ascribed to Co-M_{Td} (metal cation occupied tetrahedral site) observed at around 3 Å.[49] The plausible reason for this decrease can be the formation of Co oxyhydroxide species during OER. The distance between Co atoms and their neighbouring metal atoms are still much larger than 2.5 Å, suggesting that the surface Co is in octahedral position but the Co in the bulk remains in the tetrahedron. Indeed, as observed by HRTEM, this newly formed surface is likely amorphous without long-range order.[47,50] Altogether, these results suggest that higher applied potential is aiding the leaching of Cr, thus creating cation vacancies which result in

enhanced evolution of surface Co into Co oxyhydroxide species. As analysed by the X-ray photoelectron spectra (XPS), the Co spectra for $CoCr_2O_4$ activated at 1.6 and 1.64 V exhibit an additional peak at 781.3 eV and a satellite signal at 786.3 eV, indicative of the appearance of $Co^{3+\sim4+}$ surface species on the surface after activation (Figure 3c and Supporting Information Figure S24).[51–53] Besides, the $CoCr_2O_4$ catalyst subjected to 1.64 V vs. RHE possesses more fraction of $Co^{3+\sim4+}$ on the surface compared to that activated at 1.6 V vs. RHE, which is a result of more Cr leaching and more surface Co participating in surface reconstruction. The surface Co species are also observed for Act-$CoCr_2O_4$ by a surface sensitive soft XAS technique. Co L3 and L2 peak positions in Act-$CoCr_2O_4$ spectrum shift to the position as CoOOH, which is at higher energy region compared to Pri-$CoCr_2O_4$ (Figure 3d). This suggests a higher oxidation state for Co species on the newly formed surface after activation (Figure 3e). To understand how high oxidation state for Co ions is promoted along with Cr leaching under increasing activation potential, further characterizations on surface lattice oxygen were carried out.

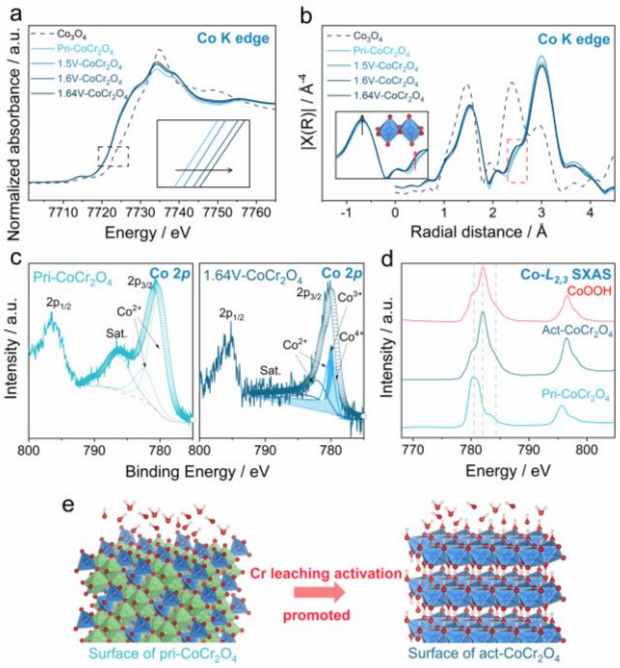

Figure 3. Evaluation of surface-active species for Act-$CoCr_2O_4$. (a) Normalized Co K-edge XANES spectra for Pri-$CoCr_2O_4$ and activated $CoCr_2O_4$ after CA at a potential of 1.5/1.6/1.64 V for 7 hours. (b) FT-EXAFS spectra for Co K-edge for Pri-$CoCr_2O_4$ and activated $CoCr_2O_4$ after CA at a potential of 1.5/1.6/1.64 V for 7 hours. (c) XPS of Co 2p regions for the surface of Pri-$CoCr_2O_4$ (left panel) and $CoCr_2O_4$ activated at 1.64V (right panel). Fittings of experimental spectra obtained for $CoCr_2O_4$ are shown in coloured lines. (d) Co L-edge soft XAS spectra for Pri-$CoCr_2O_4$ and Act-$CoCr_2O_4$ with CoOOH as reference. (e) Scheme of $CoCr_2O_4$ surface before OER testing (left panel) and after OER activation in alkaline solution (right panel).

Leaching of lattice oxygen. The O 1*s* XPS spectra of $CoCr_2O_4$ samples can be deconvoluted into different contributions, with the signals at 530 eV and 531.5 eV reflecting the presence of lattice oxygen and hydroxide ions, respectively[51,54,55,56] (Figure 4a and Supporting Information Figure S26). Around 50% of the surface oxygen species for the Pri-$CoCr_2O_4$ and $CoCr_2O_4$ activated at 1.5 V are composed of lattice oxygen. However, the proportion of lattice oxygen decreases to 29.5% by holding potential at 1.6 V vs RHE and even less for that at 1.64 V vs RHE (Figure 4b and Supporting Information Figure S27). This shows that lattice oxygen is consumed at a high potential where Cr leaching occurs at the expense of hydroxide species deposited upon surface reconstruction (Supporting Information Figure S27), agreeing with our TEM-EDS line scan and XAS analysis.

To understand whether the promoted surface species formation originates from the participation of lattice oxygen to the OER, as previously observed for numerous catalysts[4,23,58,59], a gas chromatography–mass spectrometry (GC-MS) has been conducted after OER for ^{18}O labelled Pri-$CoCr_2O_4$ and Act-$CoCr_2O_4$ (Supporting Information Figure S28 and Figure S29). Doing so, it is found that both ^{18}O labelled Pri-$CoCr_2O_4$ and Act-$CoCr_2O_4$ after OER in $K^{16}OH$ do not release $^{18}O_2$ or $^{16}O^{18}O$ during OER (Supporting Information Figure S30 and Figure 4c). This observation shows that the oxygen evolved is not from the lattice oxygen in $CoCr_2O_4$ either with activation or without activation. By detecting the evaporated liquid solution after OER in $K^{16}OH$ for ^{18}O labeled Act-$CoCr_2O_4$, ^{18}OH and $H_2{}^{18}O$ are observed besides ^{16}OH and $H_2{}^{16}O$ (Figure 4d). This implies that lattice oxygen in Act-$CoCr_2O_4$ dissolves into the KOH solution after OER. This loss of lattice oxygen may originate from the leaching of soluble Cr^{6+} species.[60,61] Hence, by using ion chromatography (IC), a representative peak for Cr^{6+} ion[62] has been observed in the KOH solution after OER of Act-$CoCr_2O_4$ (Supporting Information Figure S31). This indicates that chromate $(CrO_4)^{2-}$ are released during oxidation of Cr^{4+} species at OER potentials, that phenomenon becoming greater at higher potentials. Indeed, at 1.5 V vs RHE, the content of lattice oxygen is almost the same as that in Pri-$CoCr_2O_4$ (Supporting Information Figure S26), while at 1.6 V vs RHE above the OER onset potential, lattice oxygen starts to be detected in the alkaline electrolyte as the result of the formation of chromate $(CrO_4)^{2-}$ soluble species. The continuous dissolution of Cr ions thus leaves a large amount of cation vacancies and oxygen vacancies (O_{vac}), exposing the tetrahedral Co from the surface towards the bulk. This is supported by the loss of lattice oxygen on the surface outweighing the gain in OH^- ions, as shown in Figure 4b and Supporting Information Figure S27. This difference is a result of the O_{vac} formed on the surface. As observed by O K-edge soft XAS spectra in Figure 4e, the change in O K prepeak intensity indicates the change in metal-oxygen bonding covalency or the formation of defects in the structure. A large number of O_{vac} on the surface of Act-$CoCr_2O_4$ creates favorable conditions for the formation of amorphous Co oxyhydroxide layer[22] without long-range order by absorbing the OH^- ions from the electrolyte. This gives rise to a much enhanced OER activity (Supporting Information Figure S10), as manifested by three orders of magnitude increase in turnover frequency (TOF) for Act-$CoCr_2O_4$ (Experimental methods and Supporting Information S30) when compared to CoOOH (Supporting Information S31). For CoOOH, there are more electrochemically accessible sites, however, not all sites electrochemically accessible are OER active. While for Act-$CoCr_2O_4$, Cr leaching and surface modulation not only increases the number of active sites but also the intrinsic activity per active site for Co (Supporting Information Figure S10). That behavior is also different from NiFeOOH-Cr as reported by Xu et.al. [64] When

Cr leaches, only the number of active sites increases but not the intrinsic activity per site.

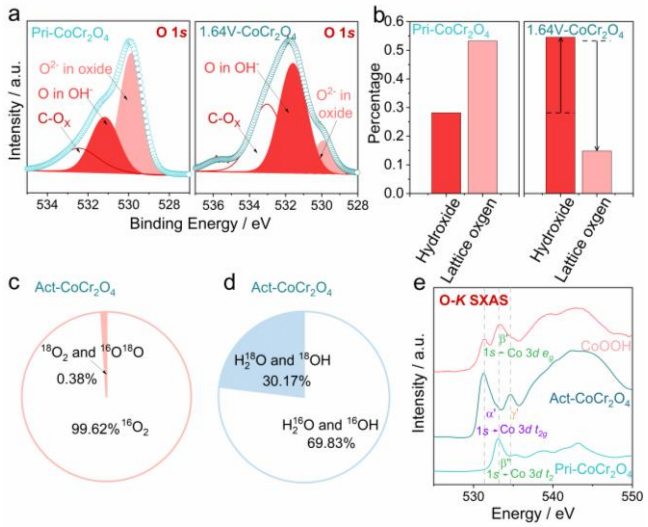

Figure 4. Probing lattice oxygen leaching for Act-$CoCr_2O_4$. (a) XPS of O 1*s* regions for Pri-$CoCr_2O_4$ surface (left panel) and $CoCr_2O_4$ activated at 1.64V (right panel). Fittings of experimental spectra obtained for $CoCr_2O_4$ are shown in coloured lines and can be divided into three regions, which are O in C-O_X, O in OH^- and O^{2-} in oxides.[55,56,57] The regions corresponding to O^{2-} in oxides are filled with light red colour. (b) Percentage of oxygen contained in C-O_X, OH^- and oxides for Pri-$CoCr_2O_4$ and $CoCr_2O_4$ activated at 1.64V. (c) The percentage of $^{16}O_2$ and $^{18}O_2$ & $^{16}O^{18}O$ detected by GC-MS after OER of ^{18}O labelled Act-$CoCr_2O_4$ in $K^{16}OH$. (d) The percentage of $H_2{}^{16}O$ & ^{16}OH and $H_2{}^{18}O$ & ^{18}OH detected by GC-MS after evaporating the liquid after OER of ^{18}O labelled Act-$CoCr_2O_4$ in $K^{16}OH$. (e) O *L*-edge soft XAS spectra for Pri-$CoCr_2O_4$ and Act-$CoCr_2O_4$ with CoOOH as reference.

Leaching and Surface Reconstruction Mechanism. To further probe the effect of activation potential on the possible reaction paths for Pri-$CoCr_2O_4$ and Act-$CoCr_2O_4$, pH-dependent experiments were conducted in 0.1M / 0.3M / 1M KOH. The OER activity measured of Pri-$CoCr_2O_4$ and $CoCr_2O_4$ activated at 1.54 V vs RHE shows no pH dependence (Supporting Information Figure S35 and S36). This suggests that, when the activation of $CoCr_2O_4$ is not triggered, a conventional adsorbate evolving mechanism (AEM) with four concerted proton-electron transfer on the surface metal-ion center[63] dominates (Figure 5a) and a very stable surface is formed under OER. Nevertheless, the activity for $CoCr_2O_4$ activated at 1.54 V vs RHE, though negligible, is a bit higher than that for Pri-$CoCr_2O_4$. From the surface redox peaks position and TEM-EDS results, the surface is found to be covered with Cr atoms. Hence, while its thickness is certainly very limited, a Cr oxyhydroxide surface layer may form after activation at a rather low potential. However, a pH-dependent OER activity is observed for $CoCr_2O_4$ activated at 1.64 V vs RHE (Supporting Information Figure S37), a dependence which is even greater after activation at 1.7 V vs RHE (Supporting Information Figure S38). This agrees with the change in Tafel slope when a potential higher than 1.6 V is applied. The pH dependence for the anodic current is often associated with lattice oxygen oxidation activity[23]. As mentioned by May et al., surface reconstruction is likely to occur via lattice oxygen participating mechanism when the O 2*p* center (relative to Fermi level) is higher than -2.2 eV[32]. The O 2*p* band center of $CoCr_2O_4$ is computed to be at -1.803 eV by DFT calculations, indicating the redox activity of lattice oxygen upon anodic polarization. However, the surface reconstruction here is very different from the one observed after the participation of lattice oxygen to the OER.[32] Here, lattice oxygen in Act-$CoCr_2O_4$ leaches concomitantly with Cr when applying a high anodic potential (>1.56 V), leaving cation and anion vacancies on the surface. Doing so, the tetrahedrally coordinated Co cations on the surface of Pri-$CoCr_2O_4$ are isolated from each other. Since there are no adjacent metal centers bridged by oxo groups, the oxygen release following the direct coupling of dual-metal sites, as previously observed for amorphous oxyhydroxides, does not happen with cations in tetrahedral sites. Hence, $Co^{2+}{}_{Td}$ has always been considered to be an OER inactive site.[19,20] The dissolution of $Cr^{3+}{}_{Oh}$ cation stimulated at the high anodic potential in Act-$CoCr_2O_4$, fortunately, facilitates the $Co^{2+}{}_{Td}$ cations to form an octahedrally coordinated oxyhydroxide layer which does not have long-range order. This can be either $Co^{2+}{}_{Td}$ cations first lose their coordination and dissolve at the interface, then quickly re-deposit under OER conditions back onto the surface, or $Co^{2+}{}_{Td}$ cations directly form into Co oxyhydroxide (Figure 5b). The highly lacunar surface favors the absorption of hydroxides and surface Co species when compared to CoOOH film[42]. Since the surface is full of defects and oxygen vacancies are created by Cr leaching, a non-concerted proton-electron transfer[63] is demonstrated in Figure 5c and which presumably arises from the chemical exchange of hydroxyls species into the surface oxygen vacancies. The success in promoting surface reconstruction by controllable leaching of Cr in $CoCr_2O_4$ in this work makes a good example of intentional surface regulation. When the activation potential is high enough, Cr leaching is initiated. The release of lattice oxygens tremendously increases when Cr is leaching out at increasing potentials, leading to the formation of vacancies and defects and the reorganization of Co cations into oxyhydroxide. The Cr leaching not only facilitates the exposure of more surface-active sites but also increases the intrinsic activity per site, which gives rise to the promoted OER activity (Figure 5b). This intentionally controlled leaching for Act-$CoCr_2O_4$ thus enables Co in tetrahedral sites to contribute to OER by forming favorable edge-shared octahedra without long-range ordering. The only short range amorphization on the surface enables the bulk structure to be stable under more than 24 hours of stability test (Supporting Information Figure S39).

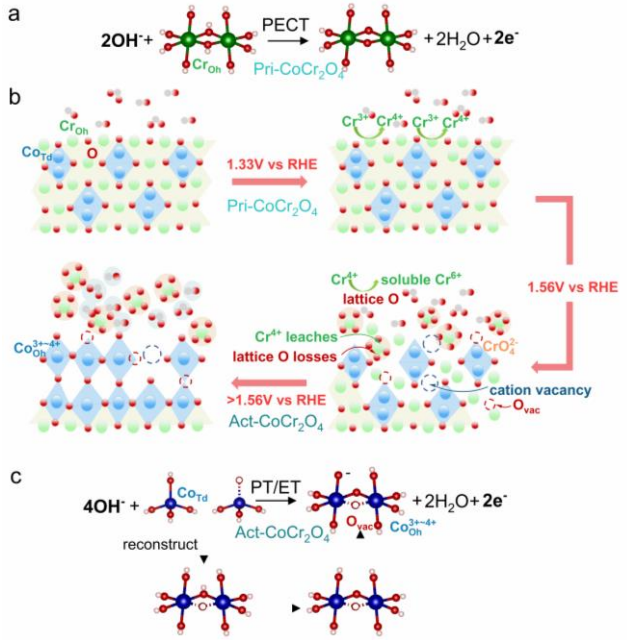

Figure 5. Activation conditions on the surface evolution mechanisms for $CoCr_2O_4$. (a) Proton electron concerted transfer for Pri-$CoCr_2O_4$. (b) Scheme of $CoCr_2O_4$ surface change before OER testing after being applied increased potentials. (c) Proton electron non-concerted transfer for Act-$CoCr_2O_4$.

Conclusion

In summary, we have demonstrated the promotion of surface reconstruction for $CoCr_2O_4$ via controllable leaching of Cr. This surface reconstruction by Cr leaching has been investigated by CA studies and characterization techniques such as ICP, TEM-EDS, XAS, XPS, and GC-MS. By activating $CoCr_2O_4$ at a potential higher than 1.56 V vs RHE, the Cr leaching can be facilitated by anodic oxidation from Cr^{4+} into Cr^{6+}, triggering the leaching of lattice oxygen anions. The Cr leaching creates vacancies and defects which allows the reconstruction of Co species on the surface to form Co oxyhydroxide which possesses different electronic structures than that of CoOOH film. Higher anodic potential triggers better performance of the catalyst by promoting the Cr leaching and lattice oxygen consumption. This newly formed surface at high activation potential exhibits more Co active sites with higher intrinsic activity per sites. The OER activity for $CoCr_2O_4$ after activation at 1.7 V vs RHE performs better than CoOOH. The catalyst is stable under 100 mA cm^{-2}_{disk} for more than 24 hours. This work brings forward the design of catalyst with transition metal cations, which have different solubility as a function of oxidation state, to act as a leaching agent allowing a controlled surface activation. Controlling the activation condition is a new strategy to induce controllable metal leaching and surface reconstruction, which can enlighten the more rational design of electrocatalysts with the controllable reconstruction ability.

Acknowledgements

This work is supported by the Singapore MOE Tier 2 (MOE2017-T2-1-009 and MOE2018-T2-2-027) and the Singapore National Research Foundation under its Campus for Research Excellence and Technological Enterprise (CREATE) programme. The authors thank the Facility for Analysis, Characterization, Testing and Simulation (FACTS) in Nanyang Technological University for materials characterization.

Keywords: OER • Controllable leaching • Surface reconstruction • Co-based material • Site occupancy

[1] Y. Jiao, Y. Zheng, M. Jaroniec, S. Z. Qiao, *Chem Soc Rev* **2015**, *44*, 2060–2086.
[2] J. Suntivich, K. J. May, H. A. Gasteiger, J. B. Goodenough, Y. Shao-Horn, *Science* **2011**, *334*, 1383–1385.
[3] H. Dau, C. Limberg, T. Reier, M. Risch, S. Roggan, P. Strasser, *ChemCatChem* **2010**, *2*, 724–761.
[4] C. Roy, B. Sebok, S. B. Scott, E. M. Fiordaliso, J. E. Sørensen, A. Bodin, D. B. Trimarco, C. D. Damsgaard, P. C. K. Vesborg, O. Hansen, I. E. L. Stephens, J. Kibsgaard, I. Chorkendorff, *Nat Catal* **2018**, *1*, 820–829.
(5) Y. Zhu, W. Zhou, Z. Shao, *Small* **2017**, *13*, 1603793.
(6) Q. Wang, K. Dastafkan, C. Zhao, *Curr Opin Electrochem* **2018**, *10*, 16–23.
(7) Y. Pi, Q. Shao, P. Wang, F. Lv, S. Guo, J. Guo, X. Huang, *Angew Chem Int Ed* **2017**, *56*, 4502–4506.
(8) M. S. Burke, M. G. Kast, L. Trotochaud, A. M. Smith, S. W. Boettcher, *J Am Chem Soc* **2015**, *137*, 3638–3648.
(9) M. E. G. Lyons, R. L. Doyle, M. P. Browne, I. J. Godwin, A. A. S. Rovetta, *Curr Opin Electrochem* **2017**, *1*, 40–45.
(10) A. C. C. Tseung, S. Jasem, *Electrochim Acta* **1977**, *22*, 31–34.
(11) S. Trasatti, *Electrochim Acta* **1984**, *29*, 1503–1512.
(12) S. Trasatti, *J Electroanal Chem Interf Electrochem* **1980**, *11*, 125-131.
(13) W. Zhou, J. Sunarso, *J Phys Chem Lett* **2013**, *4*, 2982–2988.
(14) C. Wei, Z. Feng, G. G. Scherer, J. Barber, Y. Shao-Horn, Z. J. Xu, *Adv Mater* **2017**, *29*, 1606800.
(15) H. Li, S. Sun, S. Xi, Y. Chen, T. Wang, Y. Du, M. Sherburne, J. W. Ager, A. C. Fisher, Z. J. Xu, *Chem Mater* **2018**, *30*, 6839–6848.
(16) Y. Tong, Y. Guo, P. Chen, H. Liu, M. Zhang, L. Zhang, W. Yan, W. Chu, C. Wu, Y. Xie, *Chem* **2017**, *3*, 812–821.
(17) I. Yamada, A. Takamatsu, K. Asai, T. Shirakawa, H. Ohzuku, A. Seno, T. Uchimura, H. Fujii, S. Kawaguchi, K. Wada, H. Ikeno, S. Yagi, *J Phys Chem C* **2018**, *122*, 27885–27892.
(18) R. R. Chen, Y. Sun, S. J. H. Ong, S. Xi, Y. Du, C. Liu, O. Lev, Z. J. Xu, *Adv Mater* **2020**, *32*, 1907976.
(19) S. Sun, Y. Sun, Y. Zhou, S. Xi, X. Ren, B. Huang, H. Liao, L. P. Wang, Y. Du, Z. J. Xu, *Angew Chem Int Ed* **2019**, *58*, 6042–6047.
(20) Y. Zhou, S. Sun, C. Wei, Y. Sun, P. Xi, Z. Feng, Z. J. Xu, *Adv Mater* **2019**, *31*, 1902509.
(21) J. S. Yoo, X. Rong, Y. Liu, A. M. Kolpak, *ACS Catal* **2018**, *8*, 4628–4636.
(22) E. Fabbri, M. Nachtegaal, T. Binninger, X. Cheng, B. J. Kim, J. Durst, F. Bozza, T. Graule, R. Schäublin, L. Wiles, *Nat Mater* **2017**, *16*, 925.
(23) A. Grimaud, O. Diaz-Morales, B. Han, W. T. Hong, Y. L. Lee, L. Giordano, K. A. Stoerzinger, M. T. M. Koper, Y. Shao-Horn, *Nat Chem* **2017**, *9*, 457–465.
(24) T. Wu, S. Sun, J. Song, S. Xi, Y. Du, B. Chen, W. A. Sasangka, H. Liao, C. L. Gan, G. G. Scherer, L. Zeng, H. Wang, H. Li, A. Grimaud, Z. J. Xu, *Nat Catal* **2019**, *2*, 763–772.
(25) L. Trotochaud, S. W. Boettcher, *Scr Mater* **2014**, *74*, 25–32.
(26) H. Jiang, Q. He, Y. Zhang, L. Song, *Acc Chem Res* **2018**, *51*, 2968–2977.
(27) R. Zhang, N. Dubouis, M. Ben Osman, W. Yin, M. T. Sougrati, D. A. D. Corte, D. Giaume, A. Grimaud, *Angew Chem Int Ed* **2019**, *58*, 4571–4575.
(28) Y. Chen, H. Li, J. Wang, Y. Du, S. Xi, Y. Sun, M. Sherburne, J. W. Ager, A. C. Fisher, Z. J. Xu, *Nat Commun* **2019**, *10*, 572.

(29) S. H. Chang, N. Danilovic, K. C. Chang, R. Subbaraman, A. P. Paulikas, D. D. Fong, M. J. Highland, P. M. Baldo, V. R. Stamenkovic, J. W. Freeland, *Nat Commun* **2014**, 5, 4191.
(30) O. Diaz-Morales, D. Ferrus-Suspedra, M. T. M. Koper, *Chem Sci* **2016**, 7, 2639–2645.
(31) N. Danilovic, R. Subbaraman, K. C. Chang, S. H. Chang, Y. J. Kang, J. Snyder, A. P. Paulikas, D. Strmcnik, Y. T. Kim, D. Myers, V. R. Stamenkovic, N. M. Markovic, *J Phys Chem Lett* **2014**, *5*, 2474–2478.
(32) K. J. May, C. E. Carlton, K. A. Stoerzinger, M. Risch, J. Suntivich, Y. L. Lee, A. Grimaud, Y. Shao-Horn, *J Phys Chem Lett* **2012**, *3*, 3264–3270.
(33) X. Cheng, B. J. Kim, E. Fabbri, T. J. Schmidt, *ACS Appl Mater Interfaces* **2019**, *11*, 34787–34795.
(34) W. T. Hong, K. A. Stoerzinger, Y. L. Lee, L. Giordano, A. Grimaud, A. M. Johnson, J. Hwang, E. J. Crumlin, W. Yang, Y. Shao-Horn, *Energ Environ Sci* **2017**, *10*, 2190–2200.
(35) J. T. Mefford, X. Rong, A. M. Abakumov, W. G. Hardin, S. Dai, A. M. Kolpak, K. P. Johnston, K. J. Stevenson, *Nat Commun* **2016**, *7*, 11053.
(36) C. Yang, C. Laberty-Robert, D. Batuk, G. Cibin, A. V. Chadwick, V. Pimenta, W. Yin, L. Zhang, J. M. Tarascon, A. Grimaud, *J Phys Chem Lett* **2017**, *8*, 3466–3472 (2017).
(37) N. C. S. Selvam, L. Du, B. Y. Xia, P. J. Yoo & B. You, *Adv Funct Mater* **2020**, 2008190.
(38) Z. J. Xu, *Sci China Mater* **2020**, *63*, 3–7.
(39) C. Yang, O. Fontaine, J. M. Tarascon, A. Grimaud, *Angew Chem Int Ed* **2017**, *129*, 8778–8782.
(40) D. Carta, M. F. Casula, A. Falqui, D. Loche, G. Mountjoy, C. Sangregorio, A. Corrias, *J Phys Chem C* **2009**, *113*, 8606–8615.
(41) M. Wang, L. Árnadóttir, Z. J. Xu, Z. Feng, *Nano-Micro Lett* **2019**, *11*, 47.
(42) Y. Lee, J. Suntivich, K. J. May, E. E. Perry, Y. Shao-Horn, *J Phys Chem Lett* **2012**, *3*, 399–404.
(43) Y. Duan, N. Dubouis, J. Huang, D. A. D. Corte, Z. J. Xu, A. Grimaud, *ACS Catal* **2020**, *10*, 4160–4170.
(44) I. Abidat, N. Bouchenafa-Saib, A. Habrioux, C. Comminges, C. Canaff, J. Rousseau, T. W. Napporn, D. Dambournet, O. Borkiewicz, K. B. Kokoh, *J Mater Chem A* **2015**, *3*, 17433–17444.
(45) L. Wu, Q. Li, C. H. Wu, H. Zhu, A. Mendoza-Garcia, B. Shen, J. Guo, S. Sun, *J Am Chem Soc* **2015**, *137*, 7071–7074.
(46) Y. Yamashita, P. Barpanda, Y. Yamada, A. Yamada, *ECS Electrochem Lett* **2013**, *2*, A75–A77.
(47) M. Risch, A. Grimaud, K. J. May, K. A. Stoerzinger, T. J. Chen, A. N. Mansour, Y. Shao-Horn, *J Phys Chem C* **2013**, *117*, 8628–8635.
(48) S. Song, J. Zhou, X. Su, Y. Wang, J. Li, L. Zhang, G. Xiao, C. Guan, R. Liu, S. Chen, H. J. Lin, S. Zhang, J. Q. Wang, *Energ Environ Sci* **2018**, *11*, 2945–2953.
(49) C. Wei, Z. Feng, G. G. Scherer, J. Barber, Y. Shao-Horn, Z. J. Xu, *Adv Mater* **2017**, *29*, 1606800.
(50) S. H. Ye, Z. X. Shi, J. X. Feng, Y. X. Tong, G. R. Li, *Angew Chem Int Ed* **2018**, *57*, 2672–2676.
(51) J. Yang, H. Liu, W. N. Martens, R. L. Frost, *J Phys Chem C* **2010**, *114*, 111–119.
(52) N. S. McIntyre, M. G. Cook, *Anal Chem* **1975**, *47*, 2208–2213.
(53) B. Liu, Y. Zhang, L. Tang, *Int J Hydrogen Energ* **2009**, *34*, 435–439.
(54) L. Liardet, X. Hu, *ACS Catal* **2018**, *8*, 644–650.
(55) K. A. Stoerzinger, W. T. Hong, E. J. Crumlin, H. Bluhm, M. D. Biegalski, Y. Shao-Horn, *J Phys Chem C* **2014**, *118*, 19733–19741.
(56) K. A. Stoerzinger, X. Renshaw Wang, J. Hwang, R. R. Rao, W. T. Hong, C. M. Rouleau, D. Lee, Y. Yu, E. J. Crumlin, Y. Shao-Horn, *Top Catal* **2018**, *61*, 2161–2174.
(57) K. A. Stoerzinger, L. Wang, H. Su, K. J. Lee, E. J. Crumlin, Y. Du, *Appl Surf Sci*, **2020**, *527*, 146919.
(58) S. Lee, K. Banjac, M. Lingenfelder, X. Hu, *Angew Chem Int Ed* **2019**, *58*, 10295–10299.
(59) Y. Surendranath, M. W. Kanan, D. G. Nocera, *J Am Chem Soc* **2010**, *132*, 16501–16509.
(60) T. L. Rinehart, D. G. Schulze, R. M. Bricka, S. Bajt, E. R. Blatchley, *J Hazard Mater* **1997**, *52*, 213–221.
(61) D. Xu, M. B. Stevens, Y. Rui, G. DeLuca, S. W. Boettcher, E. Reichmanis, Y. Li, Q. Zhang, H. Wang, *Electrochim Acta* **2018**, *265*, 10–18.
(62) R. Michalski, *Pol J Environ Stud* **2004**, *13*, 73–77.
(63) M. Görlin, J. Ferreira de Araújo, H. Schmies, D. Bernsmeier, S. Dresp, M. Gliech, Z. Jusys, P. Chernev, R. Kraehnert, H. Dau, P. Strasser, *J Am Chem Soc* **2017**, 139, 2070–2082.

Entry for the Table of Contents

$CoCr_2O_4$ activated at 1.7 V for 1.5 hours (Act-$CoCr_2O_4$) exhibits better OER activity compared to IrO_2 in alkaline solutions. Pristine $CoCr_2O_4$ is originally inactive. An activation potential larger than 1.56 V promotes the Cr leaching and lattice oxygen losses in $CoCr_2O_4$, leaving the highly defective surface for Co species to reconstruct into octahedrally coordinated $Co^{3+\sim4+}$ oxyhydroxide, which gives rise to its high performance.

Experimental Procedures

Material synthesis: $CoCr_2O_4$ was synthesized via a sol-gel technique. The precursor was made by dissolving 15mmol Co $(NO_3)_2$•$6H_2O$ (Cobalt(II) Nitrate hexahydrate, reagent grade, 98%, Sigma-Aldrich) and Cr $(NO_3)_3$•$9H_2O$ (Chromium(III) nitrate nonahydrate, Sigma-Aldrich) stoichiometrically in an aqueous solution of 3mL NH_4OH (Ammonium hydroxide, 28-30%, J.T.Baker) in 250mL beaker. 1.5g EDTA (Ethylenediaminetetraacetic acid, Alfa Aesar) and 1.5g $C_6H_8O_7$ (Citric acid, Sigma-Aldrich) were added to the mixture. The mixture was then stirred with a magnetic stirrer to obtain a homogeneous solution. It was then heated at 230 ºC overnight until a gel is formed. Then it was transferred to an oven for further heating at 250 ºC for 5 hours. Finally, the intermediate product was calcinated in a furnace at 1200 ºC for 6 hours to obtain the greenish-blue $CoCr_2O_4$ product. The method was the same for the synthesis of $ZnCr_2O_4$, with Zn $(CH_3COO)_2$•$2H_2O$ (Zinc acetate dihydrate, Sigma-Aldrich) replacing Co $(NO_3)_2$•$6H_2O$ for the precursor preparation. For the synthesis of Co_3O_4, Cr $(NO_3)_3$•$9H_2O$ was excluded for the precursor preparation and a final calcination temperature at 400ºC was adopted.

"Fe-free" alkaline solution preparation: The electrolytes used for the electrochemical studies are prepared from KOH pellets (Potassium hydroxide, semiconductor grade, pellets, 99.99% trace metals basis (Purity excludes sodium content.), Sigma-Aldrich). To avoid Fe contaminations, all measurements were conducted in plastic cells. Besides, the prepared KOH solutions at different concentrations were purified by Co $(OH)_2$ to remove the Fe impurities.[1]

Film deposition of $Co(OH)_2$: Prior to the film deposition, the glassy carbon insert for the rotating disk electrodes were cleaned by cycling 10 times in an alkaline solution with a potential range of 1.1-1.7 V. Prior to the electrochemical deposition, the electrodes were polished and ultrasonically washed by ethanol and 18.2 MΩ·cm water. Films of $Co(OH)_2$ were cathodically deposited in argon saturated 10mM $Co(NO_3)_2$ solution at a current density of 50 μA cm^{-2} for 600 s. After deposition, films were rinsed by dipping in deionized water (18.2 MΩ·cm). Prior to the OER measurements, the as-deposited electrodes were first cycled in "Fe-free" alkaline solution at 100 mV s^{-1} with a potential range of 1.1-1.7 V for 20 cycles for conditioning.[1]

Material Characterizations: The crystal structure was obtained by Bruker D8 Advance with Cu-K_α radiation (λ = 1.5418 Å). The (Brunauer-Emitter-Teller) BET specific surface areas of the materials were obtained using an ASAP Tristar II 3020. XANES and extended EXAFS characterizations were carried out at the XAFCA beamline of the Singapore Synchrotron Light Source (SSLS) with a transmission mode to obtain structural information[2]. Data reduction and data analysis were performed with the Athena software[3]. Soft XAS with total electron yield (TEY) mode is a surface sensitive technique for the characterization of surface oxidation state of catalysts. It was conducted at SINS beamline of SSLS[4] for the analysis of surface oxidation state change of $CoCr_2O_4$ before and after CA experiments. High-resolution transmission electron microscopy (HRTEM) was conducted in the Facility for Analysis Characterisation Testing and Simulation in NTU (FACTS) by a JEOL 2100F transition electron microscope with 200kV accelerating voltage. The morphology and composition of $CoCr_2O_4$ after CA experiments were compared with that of the as-synthesized $CoCr_2O_4$. TEM-EDS line scan was employed to study the change in the elemental profile from the surface to core of the material before and after electrochemical experiments.[5] The raw material was prepared by rolling carbon film-coated Cu TEM grids in the $CoCr_2O_4$ powders directly. The material after electrochemical activation were prepared by suspending it in ethanol by ultrasonication. The suspensions were then dropped onto Cu grids and dried at room temperature. Right after that, a TEM test is conducted. Besides, for the CA experiments, the $CoCr_2O_4$ was coated on the electrode without adding carbon black and Nafion. XPS measurements were performed using a PHI-5400 with Al Kα beam source (250 W) and a position-sensitive detector (PSD). The binding energy resolution is 0.8 eV, angle resolution is 45° and the detection limit is 80 K CPS. The base pressure of the measurement chamber is 3.0×10^{-7} Pa. The Ar ion (voltage 12 kV, current 4.2 mA) sputtering speed is 0.28 nm/s over an area of 300 × 300 um^2. Data from the measurements were calibrated using the adventitious carbon peak of the C 1s spectra (EB = 284.8 eV).[6] By using the Lorentz-Gaussian fitting method, the XPS spectra of O 1s, Co $2p_{3/2}$, and Cr $2p_{3/2}$ have been deconvoluted into smaller contributions as shown in Figure 3a, Supporting Information Figure S26, Figure S24, and Figure S34. GC-MS was conducted by using Agilent 5973N GCMS. The molecular mass of the gas obtained after sweeping the ^{18}O labelled Pri-$CoCr_2O_4$ and Act-$CoCr_2O_4$ in $K^{16}OH$ was analyzed. The oven temperature was set at 110°C. The air flew at a constant rate of 3 mL/min. The measurements were conducted at 100°C for 5

minutes. To analyze the composition of the liquid solution after OER of ^{18}O labelled Pri-$CoCr_2O_4$ and Act-$CoCr_2O_4$ in $K^{16}OH$, the liquid solutions were injected into the GCMS. The analytical Temperature was held at 150°C for 5 minutes for the water in the solution to evaporate and the molecular mass of the gas component was measured. IC has been conducted for the detection of anions in the solution after OER. The preconfigured Dionex ICS-1000 integrated system performed isocratic IC separations using conductivity detection. The column Temperature was set at 35°C and the flow rate was controlled at 1.2 mL/min.

Electrochemical Tests: The Oxygen evolution reactions were carried out using a three-electrode method with catalyst drop cast on glassy carbon electrode (0.196cm^2) as a working electrode, and mercury-mercury oxide electrode (Hg/HgO) and Pt plate (1×2 cm^2) serving as reference and counter electrodes, respectively. The catalysts ink used for dropping casting on the glassy carbon electrode were prepared as the following. 10 mg of catalyst was mixed with 2 mg of acetylene black (AB), 400 µl of isopropanol, 1.55ml of deionized water, and 50 µl of Nafion perfluorinated resin solution (5 wt% in H_2O). The mixture was ultrasonicated for at least 15 minutes to achieve homogenized dispersion of catalysts and carbon. 10 µl of ink was drop cast on the glassy carbon electrode and left until dry. The glassy carbon electrode was polished with alumina slurry and ultrasonicated in ethanol and water repeatedly before drop-casting. The electrochemical measurements were done by using Biologic SP 150 potentiostat. The potentials manifested in the results were converted to RHE scale by the following equation:

$E\ (vs.\ RHE) / V = E\ (vs.\ Hg/HgO) / V + E_{Hg/HgO}\ (vs.\ SHE) / V + 0.059 \times pH / V$

($E_{Hg/HgO}\ (vs.\ SHE) / V = 0.098 / V$ vs. SHE at 25°C)

To obtain the real potential applied to the catalysts, the potential calculated above should be corrected by the Ohmic drop. The Ohmic drop comes from the resistance of the electrolyte between the working and reference electrodes.

$E_{real} / V = E\ (vs.\ RHE) / V - iR$

where E_{real} is the real potential applied on the catalysts after iR correction, E_{RHE} is the measured potential in RHE scale, i is the measured current, and R is the uncompensated resistance as determined by electrochemical impedance spectroscopy (EIS). The EIS method for resistance determination is conducted by collecting the AC impedance spectra from 100 kHz to 100 mHz with a voltage perturbation of 0.6V versus reference.

The durability test of Act-$CoCr_2O_4$ was done in a 100 mL plastic baker at 100 mA/cm^2. Prior to that, 1mg sample $CoCr_2O_4$ was loaded on 2.55 m^2 carbon paper and activated at 1.7 V for 1.5 hours.

Tafel analysis: The OER activity presented in the form of a Tafel plot gives intuitive activity comparison among different catalysts.[7] It is plotted with iR-corrected potential against the logarithm of current density. A background correction was done for the current density by averaging the positive and negative scans.

The Tafel relation is shown as follows:

$\eta = a + b \log (j)$,

where η is the overpotential, which is the difference between the electrode and standard potentials ($\eta = E_{real} - E_0$), j represents the current density, and b denotes is the Tafel slope.

The fundamental relationships in electrochemical kinetics as described by the Butler-Volmer equation are the follows:

$j = j_0\{\exp(-\alpha f\eta) - \exp[(1-\alpha) f\eta]\}$,

$$f = \frac{F}{RT}$$

where α is the transfer coefficient, F is the Faraday's constant, R is the universal gas constant,

T is the absolute temperature, and j_0 is the exchange current density.

From the above equations, the following equation can be derived:

$$\eta = \frac{RT}{\alpha F} \ln (j_0) - \frac{RT}{\alpha F} \ln (j).$$

The first term corresponds to "a" in the Tafel relation. The term -RT/αF corresponds to "b", which is the Tafel slope. The slope obtained from the plot of η vs. log j can be converted into the Tafel slope which provides insight into the reaction mechanism of the catalysts.

The $CoCr_2O_4$ was cycled by cyclic voltammetry (CV) between 0.9V to 1.65V at a scan rate of 10 mV s^{-1} for the observation of OER activity and pseudocapacitance. Chronoamperometry (CA) is another electrochemical technique that measures the current response under fixed potential as a function of time. The $CoCr_2O_4$ was activated at a series of potentials using CA. The OER activities of the

sample with activation and without activation were then evaluated by CV between 0.9V to 1.65V at a scan rate of 10 mV s^{-1}. The samples prepared for TEM, XAS, ICP, XPS measurements, and pH-dependent experiments were activated by CA at the different potential of 1.5V, 1.6V, and 1.64V for 7 hours. The pH-dependent experiments were conducted by CV measurements in 0.1M KOH (pH=13.12), 0.3162M (pH=13.54) and 1M (pH=13.98) with a scan rate of 10 mVs^{-1} using three working electrodes from 0.9V to 1.65V. OER experiments were conducted to the same RHE scale to ensure that the OER overpotential with respect to the equilibrium O_2/H_2O redox potential remained identical across different values of pH[8]. Prior to the study of the contribution from lattice oxygen in Pri-$CoCr_2O_4$ and Act-$CoCr_2O_4$ on OER by GC-MS, oxygen isotopic labeling was conducted. $CoCr_2O_4$ was coated on an Au disk electrode (0.166 cm^2). An Au wire was employed as a counter electrode. The lattice oxygen in Pri-$CoCr_2O_4$ and Act-$CoCr_2O_4$ was labelled by potentiostatic holding at 1.6 V versus RHE in ^{18}O-labelled 1 M KOH solution for 10 min. After that, the electrodes were rinsed with $K^{16}OH$ prior to the OER conducted in $K^{16}OH$ with a scan rate of 2 mVs^{-1}.[9]

TOF Calculation: The TOF values are defined as the moles of O_2 evolved per mole of Co in Act-$CoCr_2O_4$ and CoOOH per second.[10] The TOFs are calculated at an overpotential of 0.37 V by the current of the CV sweeps (taken at a scan rate of 10 mV s−1) dividing by the moles of Co determined by the area of the redox peak of Co^{2+} to Co^{3+}. The details are shown in Supporting Information Figure S32 and S33.

Results and Discussion

Table 1: BET surface area of $CoCr_2O_4$ and Co_3O_4

Sample	**S_{BET} (m^2/g)**
$CoCr_2O_4$	6.3
Co_3O_4	21.4

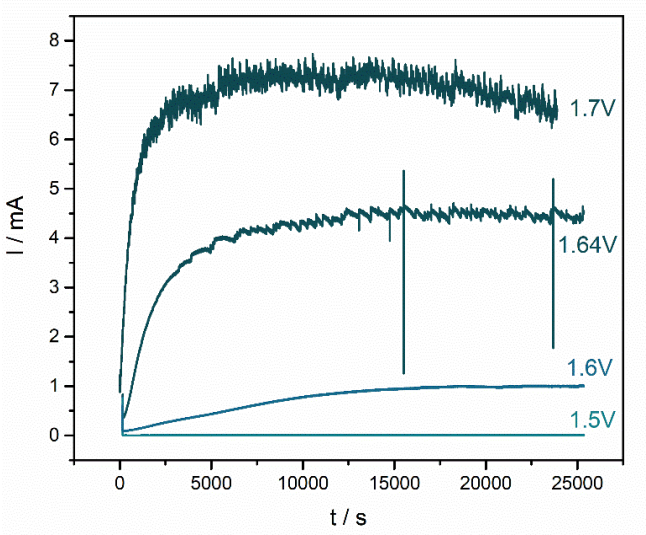

Figure S1. Chronoamperometry (CA) of $CoCr_2O_4$ at a potential of 1.5/1.6/1.64/1.7 V for seven hours. The larger the potential applied for the CA, the shorter the time for the currents to reach steady state.

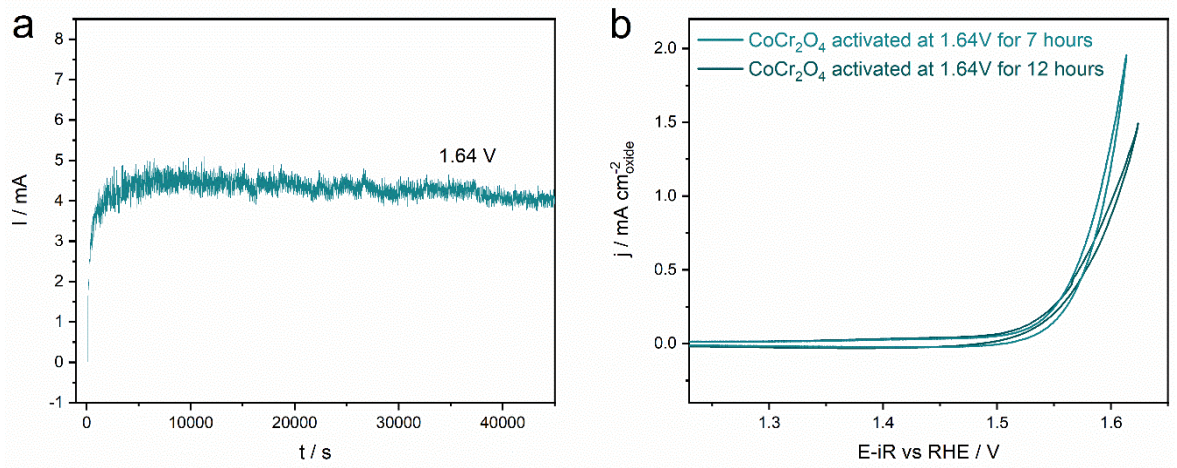

Figure S2. (a) CA of $CoCr_2O_4$ at a potential of 1.64 V for twelve hours. (b) CV after the CA of $CoCr_2O_4$ at a potential of 1.64 V for twelve hours in comparison with that after the CA of $CoCr_2O_4$ at a potential of 1.64 V for seven hours.

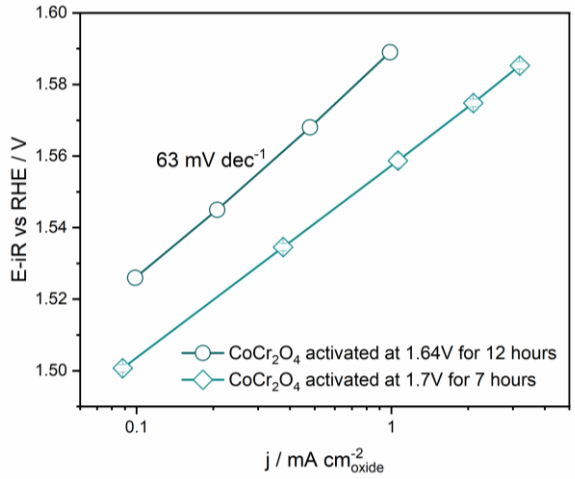

Figure S3. Tafel plot after the CA of $CoCr_2O_4$ at a potential of 1.64 V for twelve hours. Longer time for the activation by CA at lower potential does not increase the stabilized current density further and does not give raise to better activity. The Tafel plot after CA of $CoCr_2O_4$ at a potential of 1.64 V for twelve hours does not shift towards the curve for Act-$CoCr_2O_4$ activated at 1.7V for 1.5 hours. If the lower overpotentials (e.g., 1.5/1.6) were held for longer times (e.g., 14 hrs., 21 hrs.), the Tafel plots will not shift towards the curve for Act-$CoCr_2O_4$ as well. The Tafel plots at different activation potentials will not collapse onto one master curve even after very long time. This is because the lower potential is not enough to induce enough leaching quantities. Potential is the key factor for the Cr leaching and surface reconstruction, which is the main parameter influencing the activity.

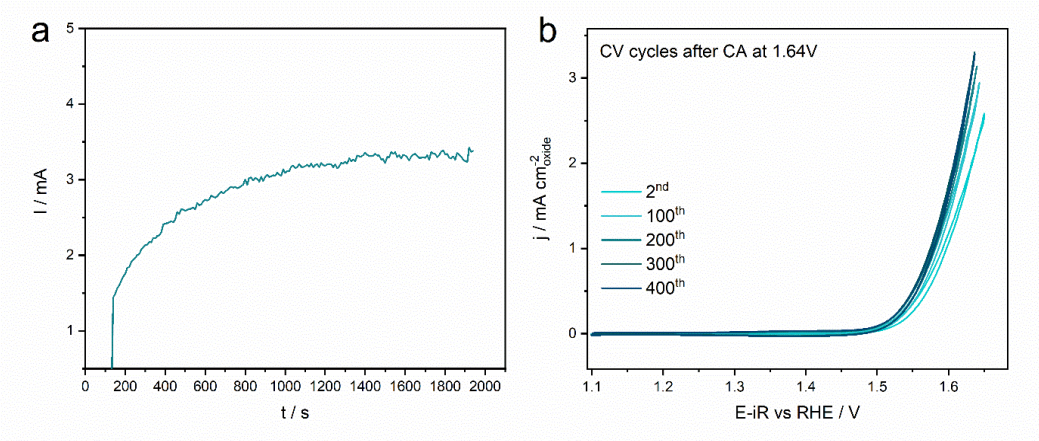

Figure S4. (a) CA of $CoCr_2O_4$ at a potential of 1.64 V for half an hour. (b) CV after CA of $CoCr_2O_4$ at a potential of 1.64 V for half an hour.

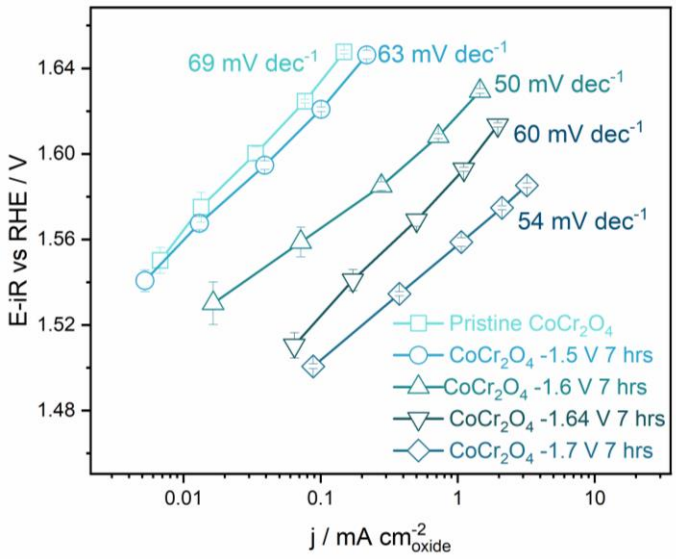

Figure S5. Tafel plots of at the 2nd cycle and after Chronoamperometry (CA) at a potential of 1.5/1.6/1.64V/1.7V for seven hours.

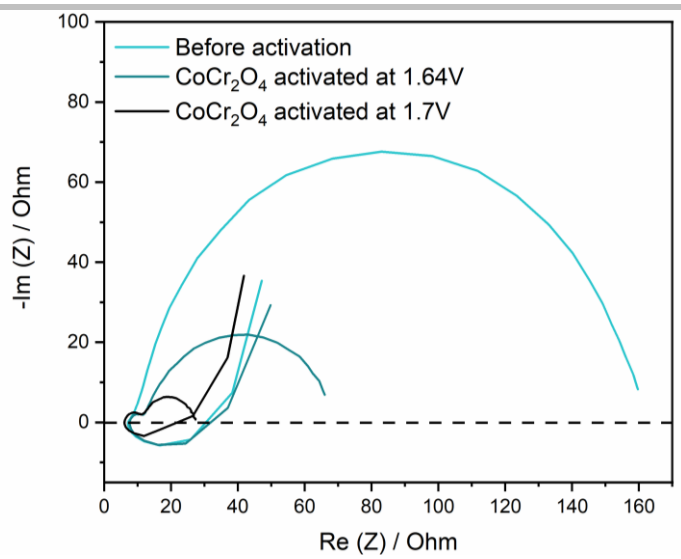

Figure S6. EIS curve of Pri-$CoCr_2O_4$, $CoCr_2O_4$ after activation at 1.64V for seven hours and Act-$CoCr_2O_4$ after activation at 1.7V for one and half hours.

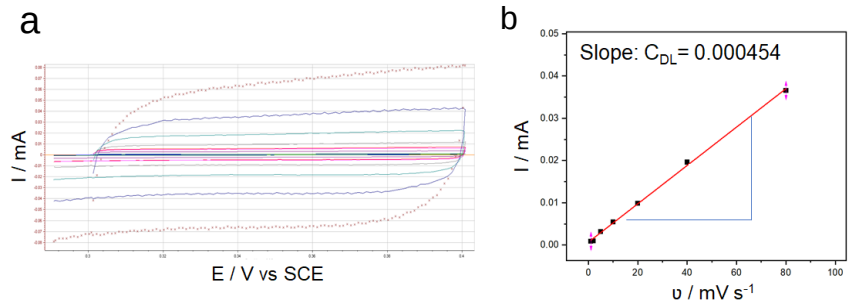

Figure S7. a) Electrochemical double layer of Pri-$CoCr_2O_4$ under different scan rates. b) Current versus scan rate for Pri-$CoCr_2O_4$.

Calculation on electrochemical surface area of Pri-$CoCr_2O_4$:

ECSA = C_{DL}/C_S

C_{DL}= i_{DL}/v= 0.000454F

C_S = 60 μF cm^{-2}

ECSA= C_{DL} / $_{CS}$ = 0.000454 / (60*10^{-6}) = 7.57 cm^2

m= 50 μg

7.57 cm^2/ 50 μg = 15.14 m^2/g

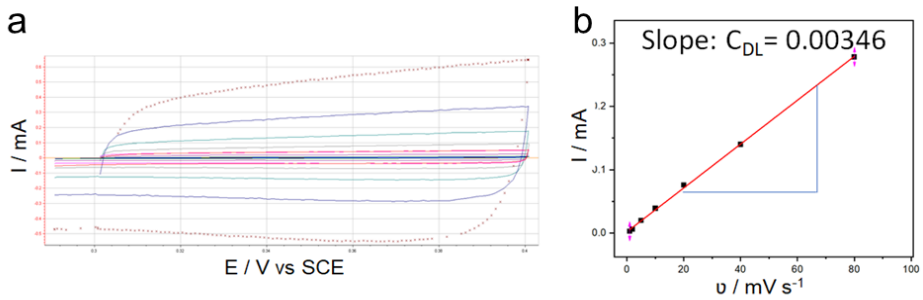

Figure S8. a) Electrochemical double layer of Act-$CoCr_2O_4$ under different scan rates. b) Current versus scan rate for Act-$CoCr_2O_4$.

Calculation on electrochemical surface area of Act-$CoCr_2O_4$:

ECSA = C_{DL}/C_S

$C_{DL}= i_{DL}/v$= 0.00346F

C_S = 60 µF cm^{-2}

ECSA= C_{DL} / $_{CS}$ = 0.00346 / (60*10^{-6}) = 57.67 cm^2

m= 50 µg

57.67 cm^2/ 50 µg = 115.3 m^2/g

The ECSA of $CoCr_2O_4$ increases from 15 to 115 m^2/g after activation, which indicates that there is increase in number of active sites after activation.

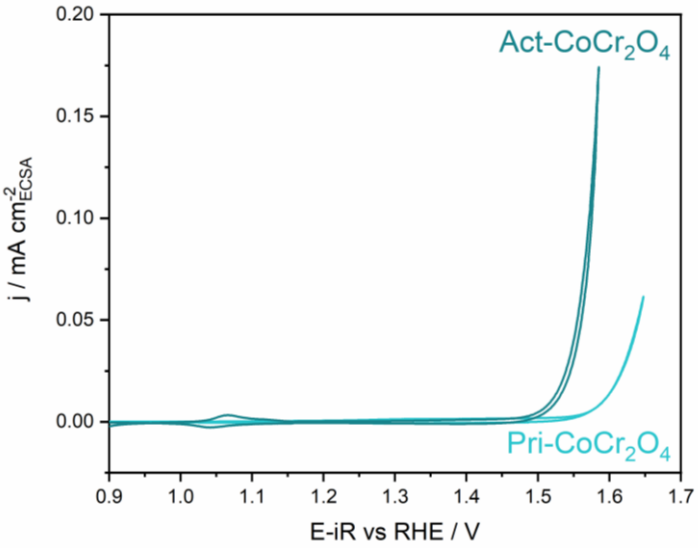

Figure S9. ECSA normalised OER activity of Pri-$CoCr_2O_4$ and Act-$CoCr_2O_4$. The current normalized by ECSA for Act-$CoCr_2O_4$ is higher than Pri-$CoCr_2O_4$, indicates that the intrinsic activity per site increases after activation. For NiFeOx[11], the substitution of Cr increases the number of active site but not the intrinsic activity per site.

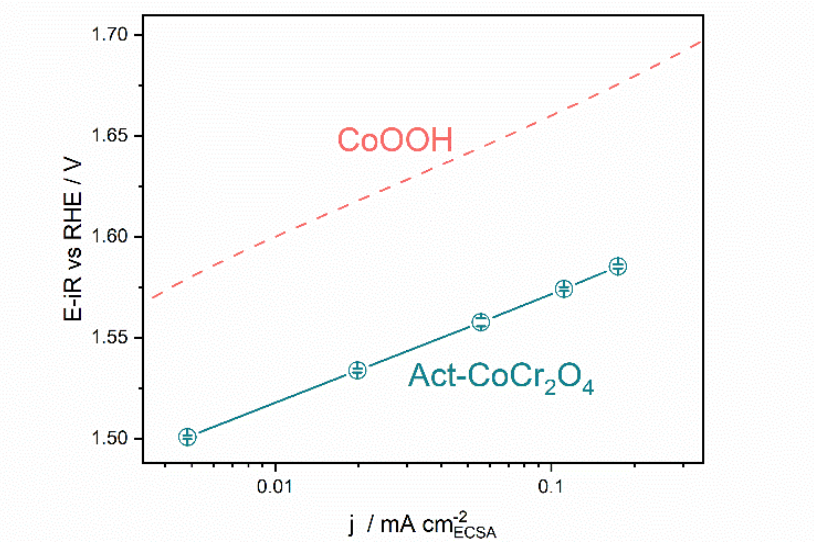

Figure S10. Comparison the specific activity between Act-$CoCr_2O_4$ and CoOOH[12].

To compare the specific activity between Act-$CoCr_2O_4$ and CoOOH[12], we have normalized the OER activity by ECSA. As shown in Figure S10, the specific activity of Act-$CoCr_2O_4$ is better than CoOOH.

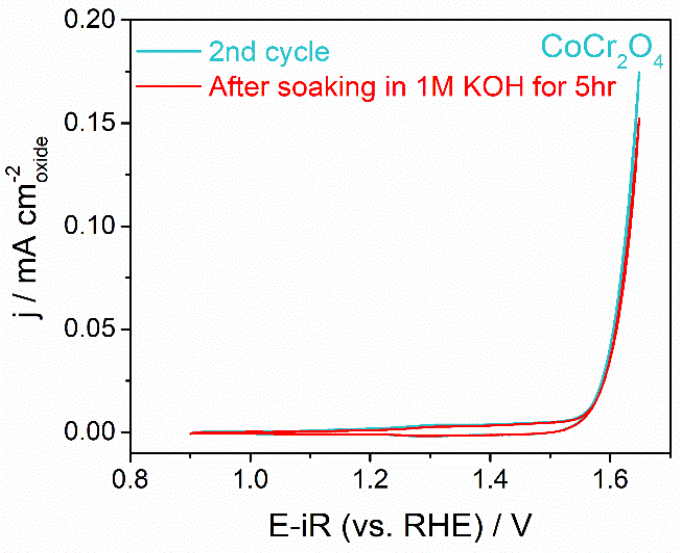

Figure S11. CV curves of $CoCr_2O_4$ at the second cycle and after soaking in 1M KOH for 5 hours.

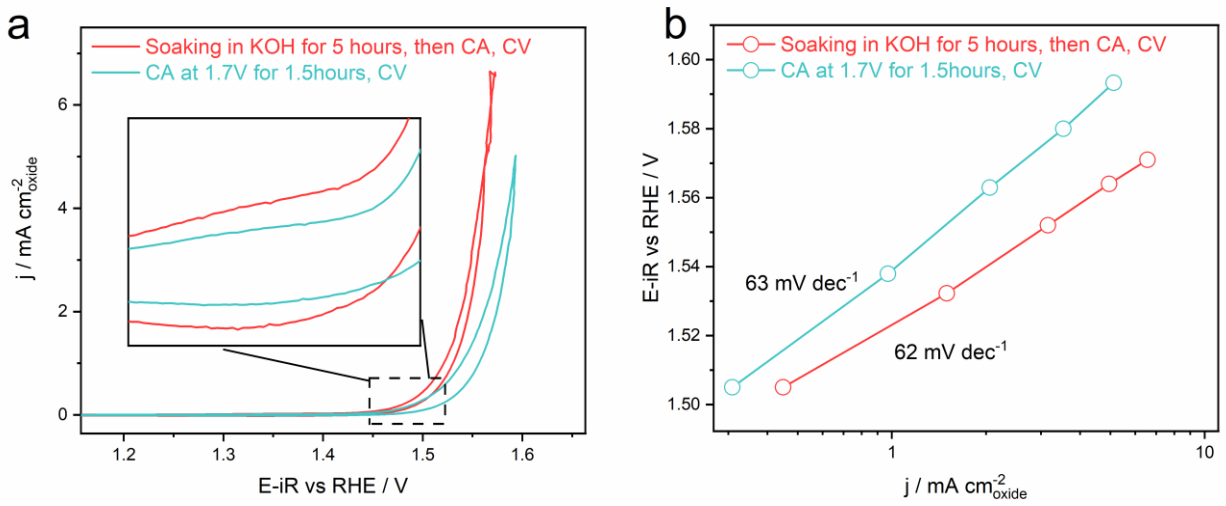

Figure S12. (a) CV curves of $CoCr_2O_4$ after CA at 1.7V for 1.5 hours with and without previously soaking in 1M KOH for 5 hours. (b) Tafel plots of $CoCr_2O_4$ after CA at 1.7V for 1.5 hours with and without previously soaking in 1M KOH for 5 hours.

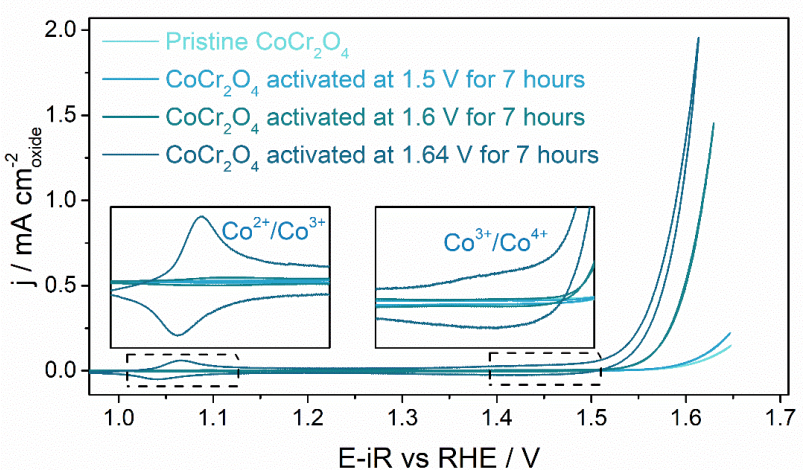

Figure S13. Electrochemical characterization on OER performance of $CoCr_2O_4$. CV curves of $CoCr_2O_4$ at the 2nd cycle and after Chronoamperometry (CA) at a potential of 1.5/1.6/1.64V for seven hours.

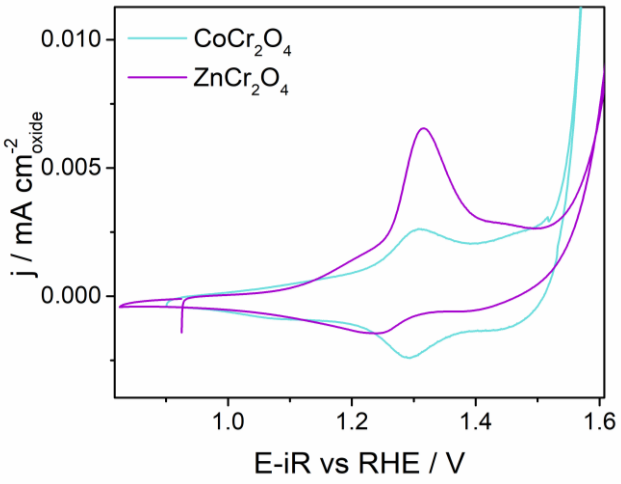

Figure S14. CV curve of $CoCr_2O_4$ and $ZnCr_2O_4$.

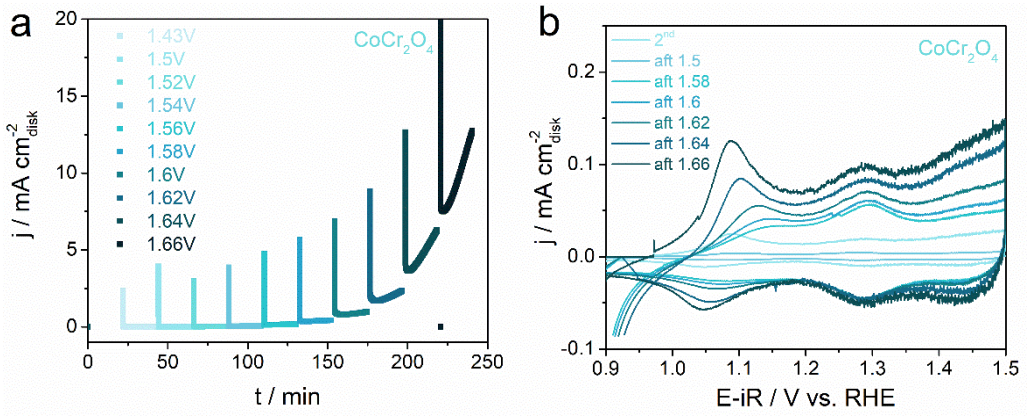

Figure S15. (a) A consecutive series of chronoamperometry (CA) at different potential from 1.43 V to 1.66 V and (b) cyclic voltammetry after CA from 1.5 V to 1.66 V for $CoCr_2O_4$.

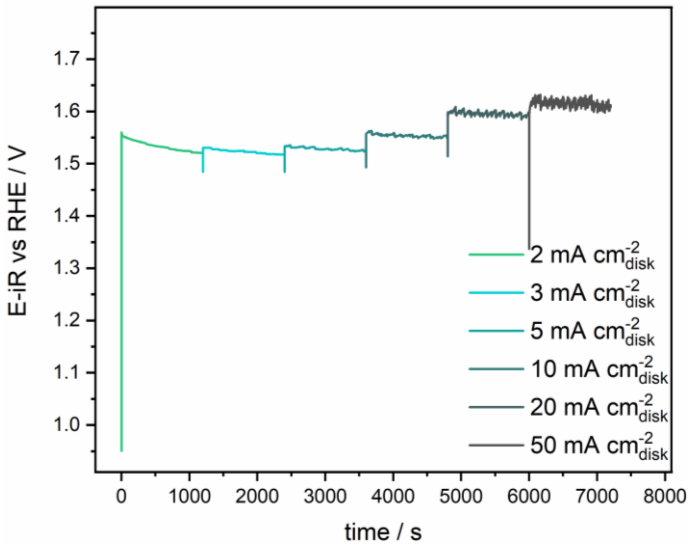

Figure S16. A consecutive series of CP at a different current density from 2 to 50 mA cm^{-2}_{disk}.

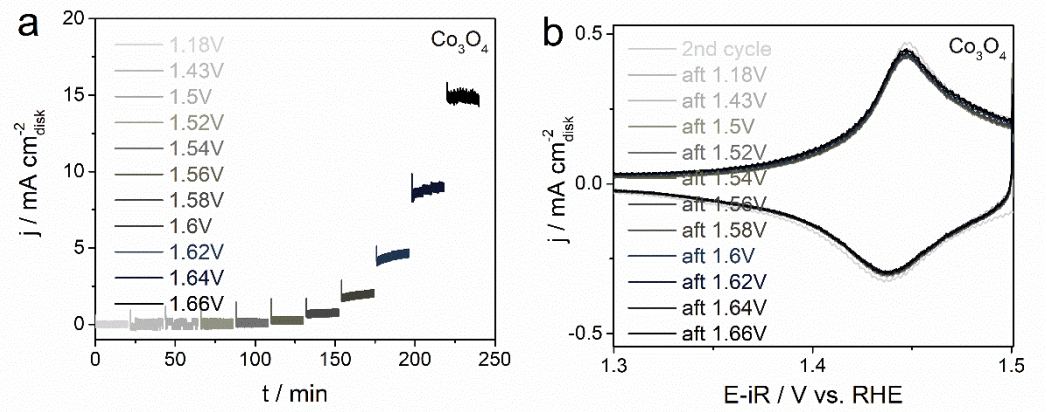

Figure S17. (a) A consecutive series of chronoamperometry (CA) at different potential from 1.18 V to 1.66 V and (b) cyclic voltammetry after CA from 1.18 V to 1.66 V for Co_3O_4.

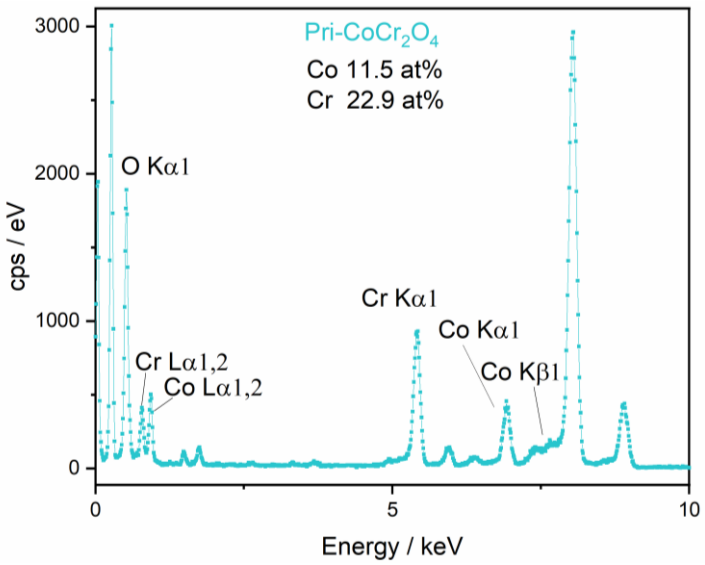

Figure S18. EDS quantification results of Pri-$CoCr_2O_4$ produced across the area from surface to bulk. Co and Cr has a stoichiometric proportion of 1:2.

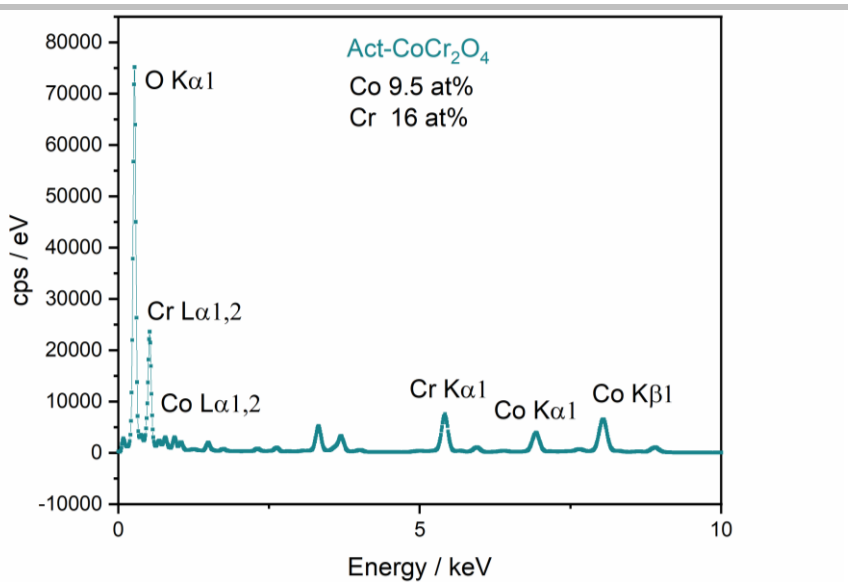

Figure S19. EDS quantification results of Act-$CoCr_2O_4$ produced across the area from surface to bulk. Co and Cr has a stoichiometric proportion more than 1:2. After activation, the ratio of Co and Cr changes. Cr is not double of Co anymore. This indicates the depletion of surface Cr.

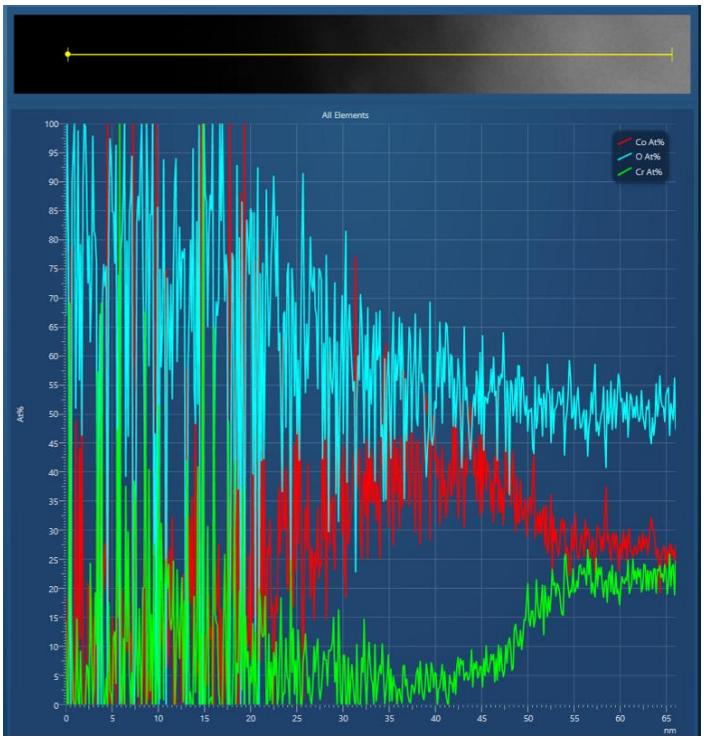

Figure S20. Quantification line scans reflecting at% varies across the surface to bulk of the elements in Act-$CoCr_2O_4$. The STEM-EDS image in Figure 2g is the intensity line scan of Act-$CoCr_2O_4$ not reflecting the at% change. Pay attention that the colors of the curves shown in Figure S19 are machine automatically generated colors (Co at% is in red, O at% is in blue and Cr at% is in green), which do not correspond to the colors of elements shown in the main text Figure 2g (Co at% is in blue, O at% is in red and Cr at% is in green). Please read the data based on the legand. The quantifiction line scans here shows a significant depletion of Cr and the abundance of Co cations on the surface of Act-$CoCr_2O_4$ activted at 1.7 V for 1.5 hours.

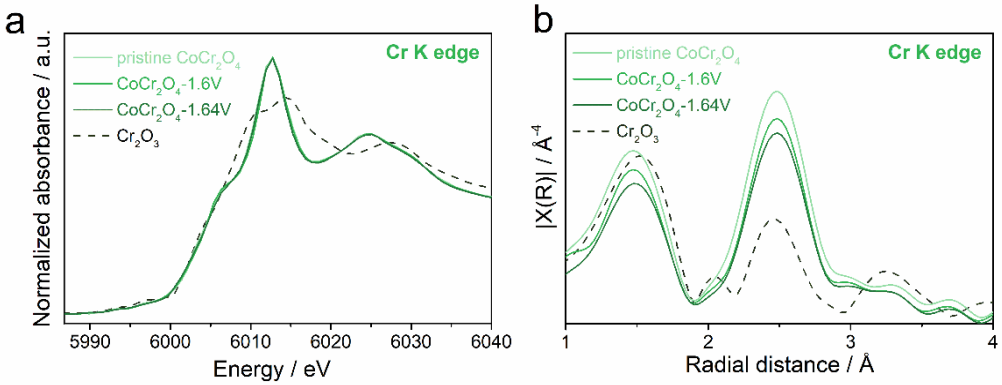

Figure S21. (a) Normalized Cr K-edge XANES spectra for pristine $CoCr_2O_4$ and activated $CoCr_2O_4$ after CA at a potential of 1.6/1.64 V (vs. RHE) for seven hours. (b) FT-EXAFS spectra for Cr K-edge for pristine $CoCr_2O_4$ and activated $CoCr_2O_4$ after CA at a potential of 1.6/1.64 V (vs. RHE) for seven hours.

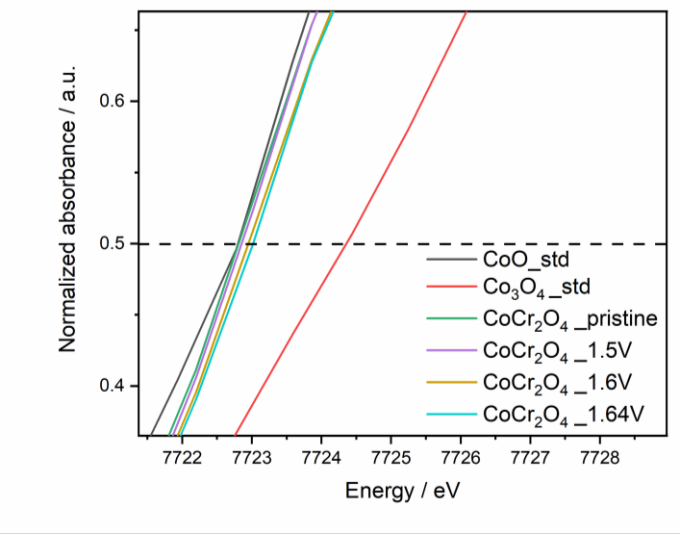

Figure S22. Merged XANES data from three different measurements of pristine $CoCr_2O_4$, activated after CA at a potential of 1.5/1.6/1.64 V (vs. RHE) for 7 hours. By using half height methods[14], the oxidation state of Co in pristine $CoCr_2O_4$, activated after CA at a potential of 1.5/1.6/1.64 V (vs. RHE) for 7 hours have been determined as 2, 2.02, 2.07, 2.09. These XANES data were obtained under transmission mode. Hence, the oxidation state is the average of the bulk and surface Co. By using XPS and SXAS, the surface Co oxidation state can be better analysed. The surface Co is more than 3+. This suggests that the Co reconstruction is only on the surface. The bulk structure is not affected much. This gives rise to the stable structure of the catalyst under long run.

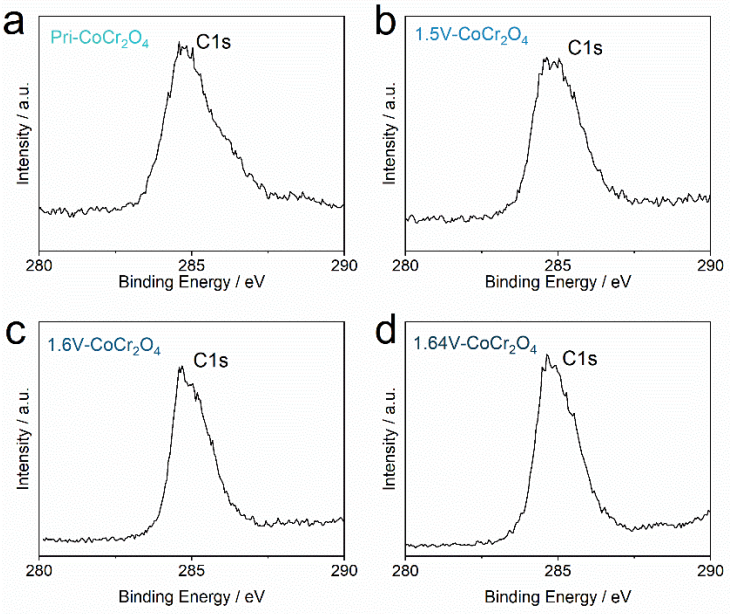

Figure S23. XPS of C 1*s* regions for $CoCr_2O_4$ surface before OER testing and after CA at a potential of 1.5/1.6/1.64 V (vs. RHE) for seven hours.[15-18] The individual edge was calibrated with a C 1s standard (284.8 eV) before analysis.

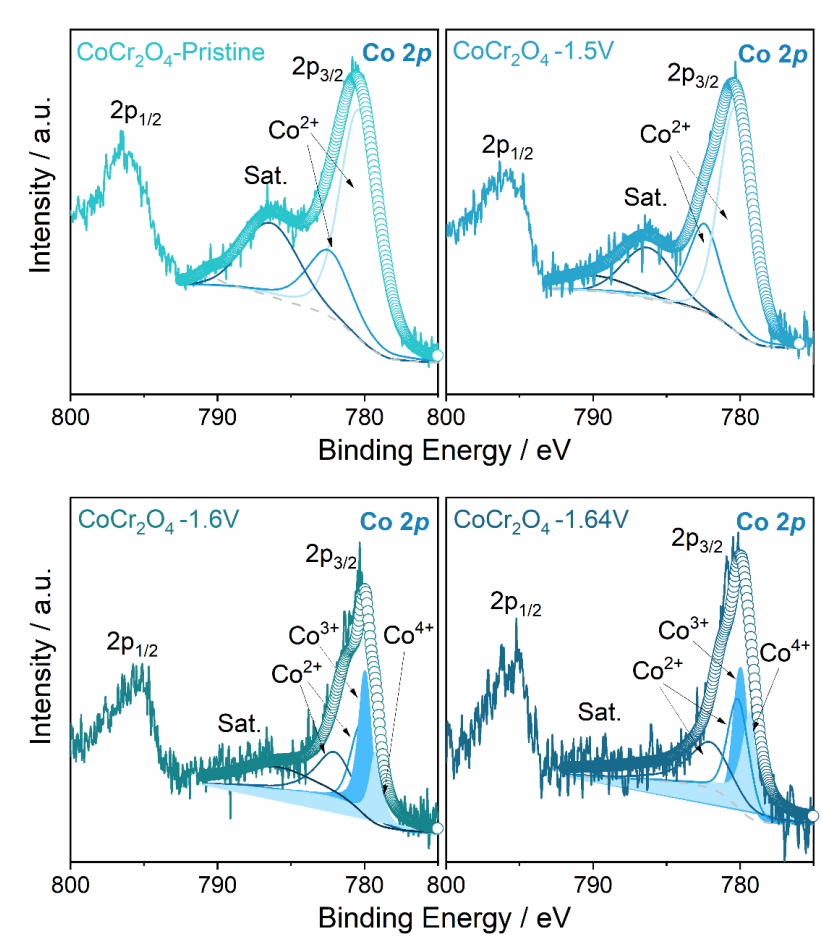

Figure S24. XPS of Co 2*p* regions for $CoCr_2O_4$ surface before OER testing and after CA at a potential of 1.5/1.6/1.64 V (vs. RHE) for seven hours. Fittings of experimental spectra obtained for $CoCr_2O_4$ are shown in coloured. All samples show deconvoluted BE signals at around 780.4 eV and 782.4 eV. However, both $CoCr_2O_4$ activated at 1.6 V and 1.64 V have an additional peak at around 781.3 eV. Pristine $CoCr_2O_4$ and $CoCr_2O_4$ activated at 1.5 V contain Co^{2+} species only. There is presence of $Co^{3\sim4+}$ species besides Co^{2+} in $CoCr_2O_4$ activated at 1.6 V and 1.64 V[19].

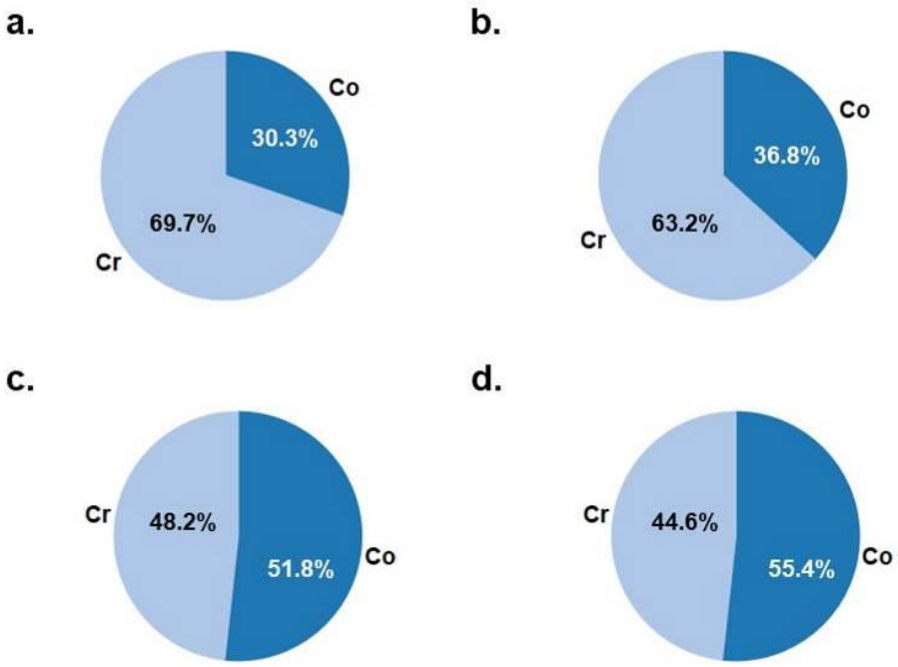

Figure S25. Based on the species per spectrum area constant derived and the deconvoluted area Co and Cr peaks excluding the satellite region, the ratio of Co and Cr was calculated for pristine $CoCr_2O_4$ (a) and $CoCr_2O_4$ after CA at a potential of 1.5 (b) /1.6 (c) /1.64 V (d) (vs. RHE). The surface ratios of Co and Cr are calculated for all samples. The pristine $CoCr_2O_4$ initially contains nearly 70% of Cr on the surface which is close to the ratio 1:2 of Co to Cr in $CoCr_2O_4$. The $CoCr_2O_4$ activated at 1.6 V and 1.64 V for 7 hours experience significant Cr leaching and more than 50% of surface Co species exposure. This phenomenon agrees well with the observations by ICP, TEM-EDS and XAS. The Cr leaching is facilitated by the potential at which the sample is activated.

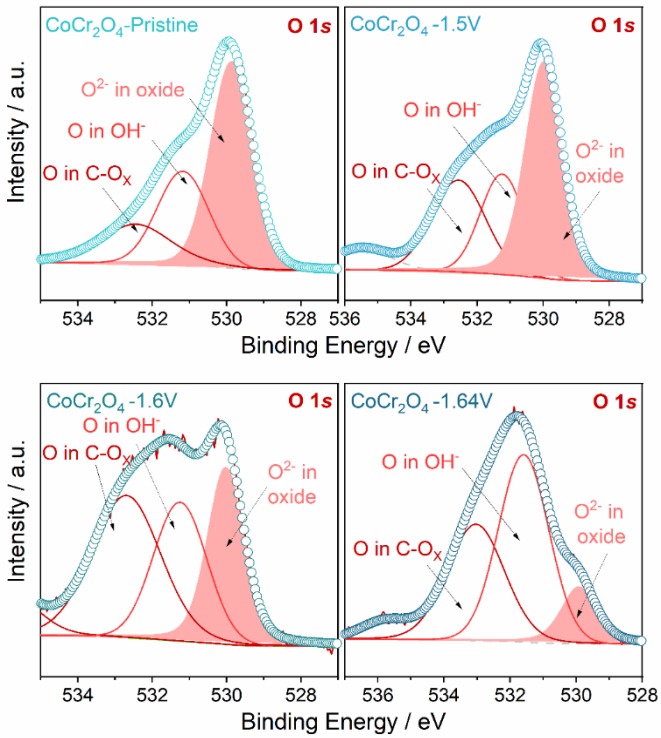

Figure S26. XPS of O 1*s* regions for $CoCr_2O_4$ surface before OER testing and after CA at a potential of 1.5/1.6/1.64 V (vs. RHE) for seven hours. Fittings of experimental spectra obtained for $CoCr_2O_4$ are shown in coloured lines and can be divided into three regions, which are O in C-O_X, O in OH^- and O^{2-} in oxides. The regions corresponding to O^{2-} in oxides are filled with light red colour. The O 1*s* spectra of $CoCr_2O_4$ samples can be deconvoluted into three different contributions. The signals at around 530 eV and 531.5 eV reflect the presence of lattice oxygen and hydroxide ions respectively.[1,19] The peak at 532.9 eV is ascribed to the presence of carbon contamination[20] which may come from the Nafion® perfluorinated solution (-CF_2–O–CF_2-) that was added to the catalyst ink during drop casting.[21]

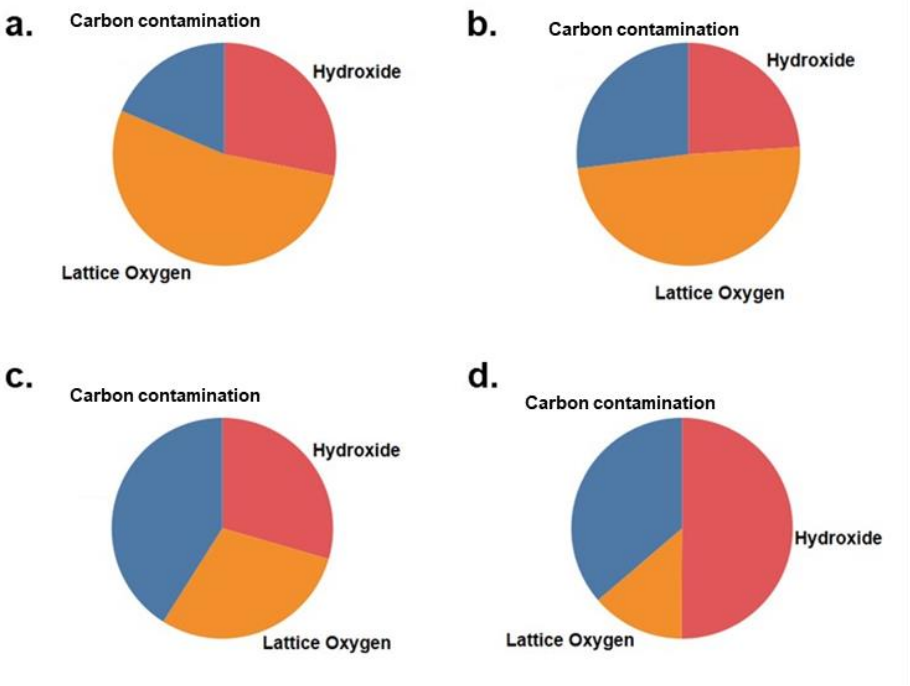

Figure S27. Distribution of different oxygen species on surface of pristine $CoCr_2O_4$ (a) and $CoCr_2O_4$ after CA at a potential of 1.5 (b) /1.6 (c) /1.64 V (d) (vs. RHE).

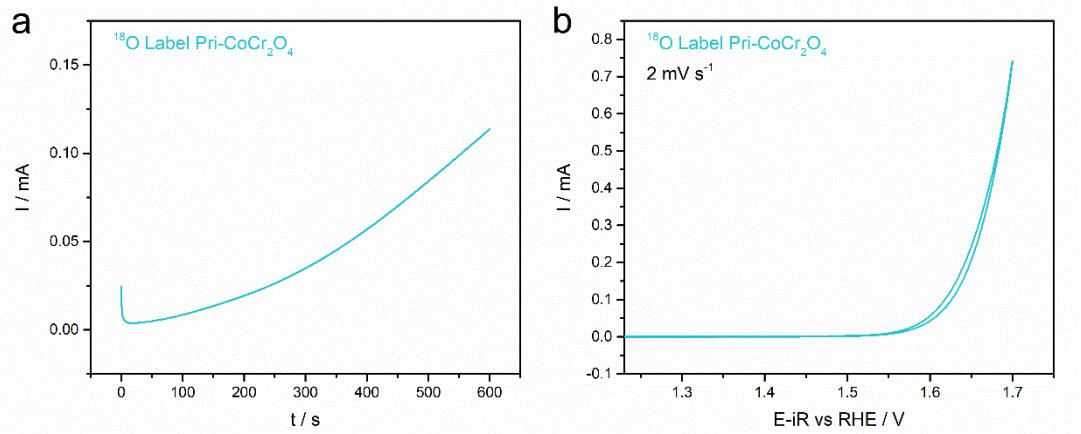

Figure S28. (a) ^{18}O labelling Pri-$CoCr_2O_4$ by potentiostatic at 1.6V vs RHE for 10 min in ^{18}O labelled 1M KOH. (b) CV of ^{18}O labelled Pri-$CoCr_2O_4$ in 1M K^{16}OH with a scan rate of 2 mVs^{-1}.

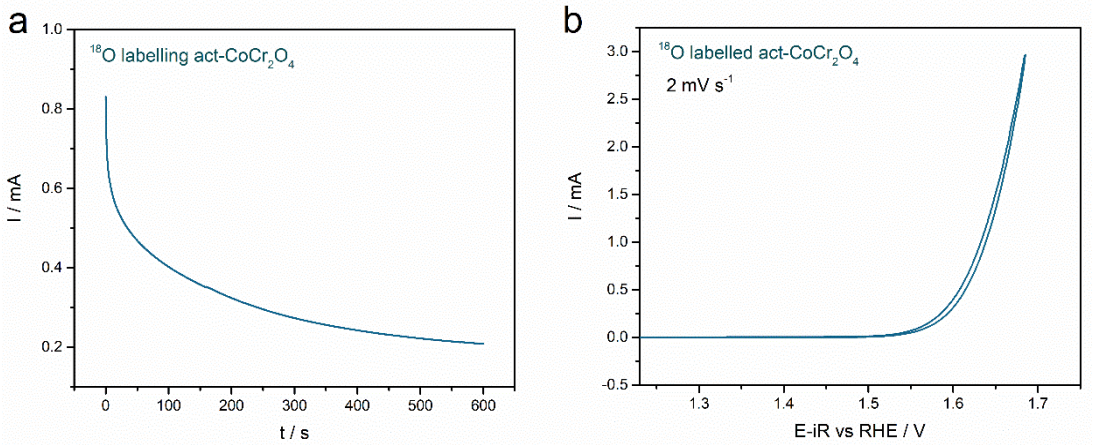

Figure S29. (a) ^{18}O labelling Act-$CoCr_2O_4$ by potentiostatic at 1.6V vs RHE for 10 min in ^{18}O labelled 1M KOH. (b) CV of ^{18}O labelled Act-$CoCr_2O_4$ in 1M K^{16}OH with a scan rate of 2 mVs^{-1}.

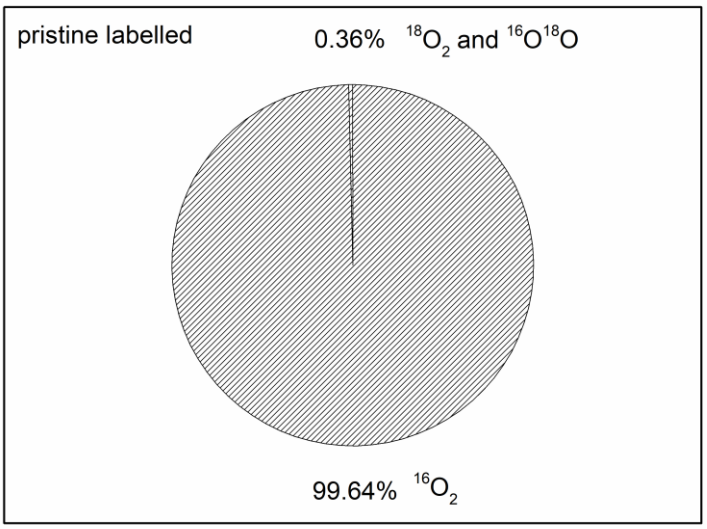

Figure S30. GC-MS for oxygen detection in ^{18}O labelled Pri-$CoCr_2O_4$ after OER.

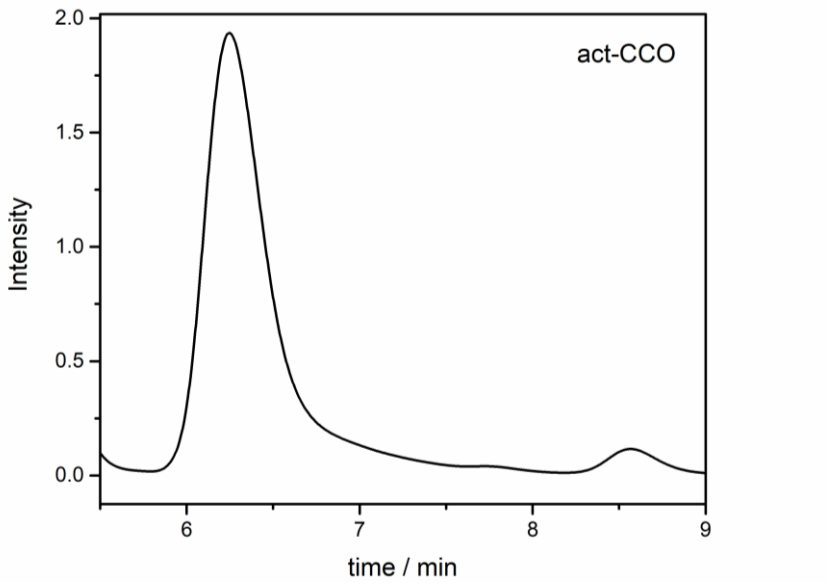

Figure S31. IC of the KOH solution after OER of Act-$CoCr_2O_4$. After OER of $CoCr_2O_4$ activated at 1.7 V (vs RHE) in 1M KOH solution, the solution contains representative peak for Cr(VI) ion which falls in t~6-7.[22] At pH < 1, the predominant species is H_2CrO_4, while as the pH is raised from pH 2 to 6, the $HCrO_4^-$ and $Cr_2O_7^{2-}$ anions prevail. At a pH > 8 only the yellow ion CrO_4^{2-} exists.[23] The Cr(VI) ion in the solution should be CrO_4^{2-}.

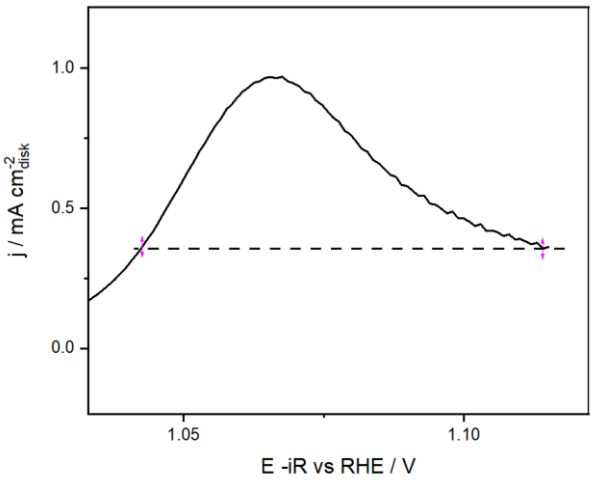

Figure S32. Determining the redox area of Act-$CoCr_2O_4$.

The TOF value for Act-$CoCr_2O_4$ is calculated as the following:

At 1.6V vs RHE:

The area of the redox for Co is: 0.047 - 0.36 * (1.11-1.04) = 0.0218 mA*V*cm^{-2}

0.0218 mA*V*cm^{-2} * 0.196 cm^2 = 0.00427 mA*V

The scan rate is at 10 mVs^{-1}

The current at 1.6 V (vs.RHE) is 19.59 mA

TOF=Current at 1.6V/ (area of redox peak/scan rate) = 45.8 s^{-1}

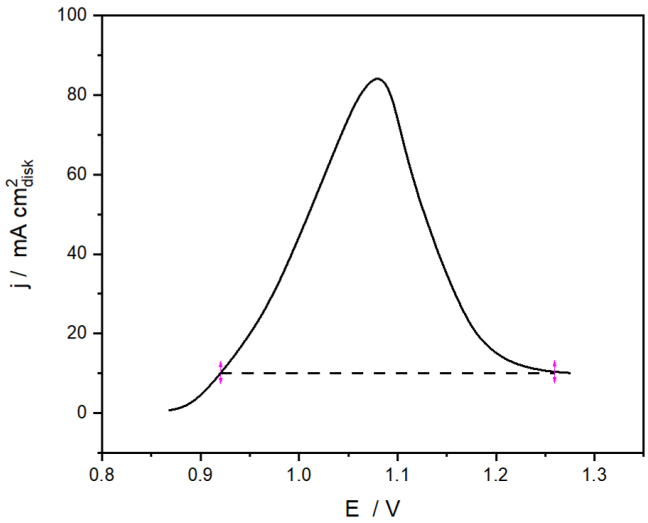

Figure S33. Determining the redox area of CoOOH.

The TOF value for CoOOH is calculated as the following:

At 1.6V vs RHE:

The redox area for Co is: 13.49-10.15*(1.26-0.92) = 10.04 mA*V*cm^{-2}

10.04 mA*V*cm^{-2} * 0.196 cm^2 =1.97 mA*V

The scan rate is at 10 mVs^{-1}

The current at 1.6 V (vs. RHE) is 3.42 mA

TOF=Current at 1.6V / (area of redox peak/scan rate) = 0.0174 s^{-1}

The area of the redox area for Co indicates the electrochemically accessible sites. The Co redox area for Act-$CoCr_2O_4$ is 0.0218 mA*V*cm^{-2} and 10.04 mA*V*cm^{-2} for CoOOH. It means that there are more electrochemically accessible sites for CoOOH. However, the activity is much lower, hence, not all these electrochemically accessible sites eventually contribute to the OER activity for CoOOH. Hence, the TOF is much less than that for Act-$CoCr_2O_4$.

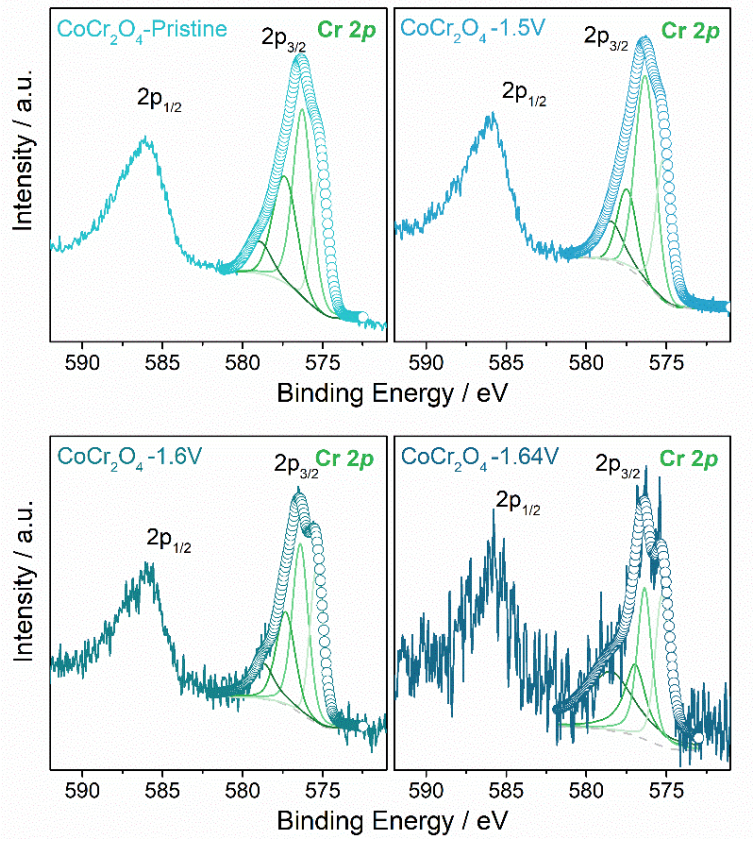

Figure S34. XPS of Cr 2*p* regions for $CoCr_2O_4$ surface before OER testing and after CA at a potential of 1.5/1.6/1.64 V (vs. RHE) for seven hours. Fittings of experimental spectra obtained for $CoCr_2O_4$ are shown in coloured. The Cr $2p_{3/2}$ XPS spectrum for all the $CoCr_2O_4$ samples peaked at 576.4eV indicate the presence of Cr^{3+} in octahedral sites of the spinel.[20,24] The peak can be further resolved into four smaller peaks due to multiplet splitting for unpaired electrons in Cr^{3+}.[25,26] However, there might be some Cr^{3+} that exist in all samples as CrOOH peak at 577.3 eV may be overlapped by the peaks of Cr^{3+} belonging to $CoCr_2O_4$ lattice. The absence of a peak at around 578.2 eV suggests that there is no Cr^{6+} species present on the surface.[20,24]

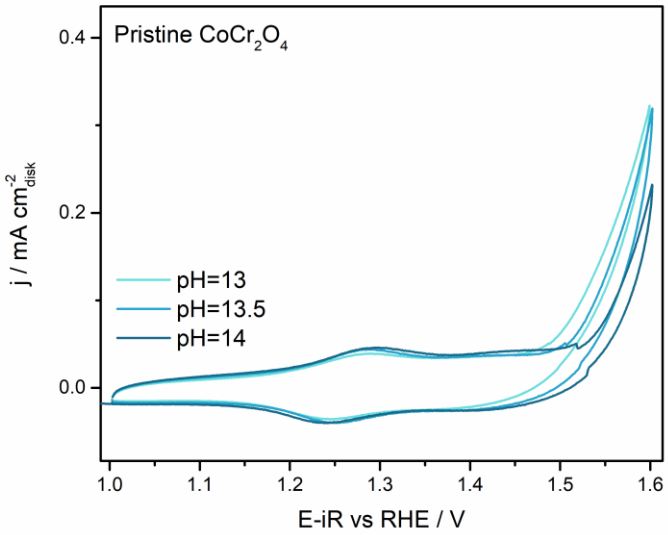

Figure S35. pH dependent OER activity for pristine $CoCr_2O_4$.

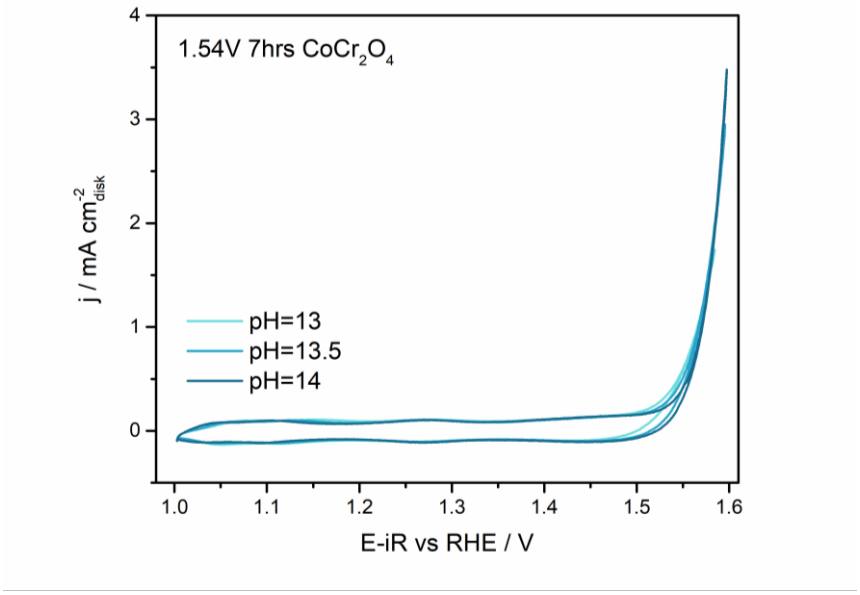

Figure S36. pH dependent OER activity for $CoCr_2O_4$ after CA at 1.54V for 7 hours.

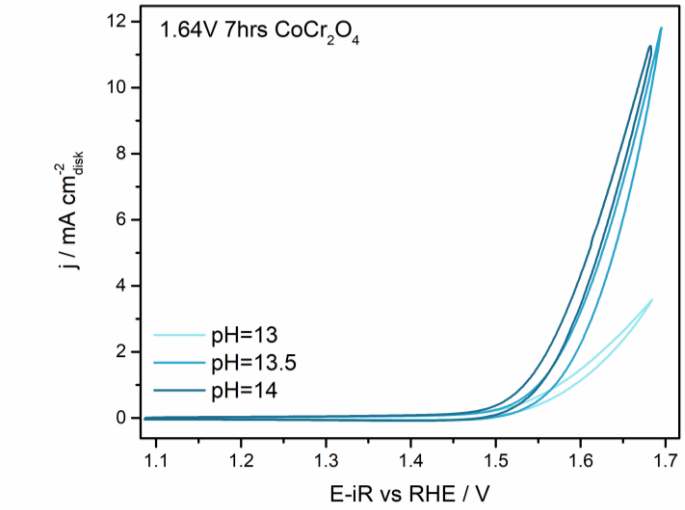

Figure S37. pH dependent OER activity for $CoCr_2O_4$ after CA at 1.64V for 7 hours.

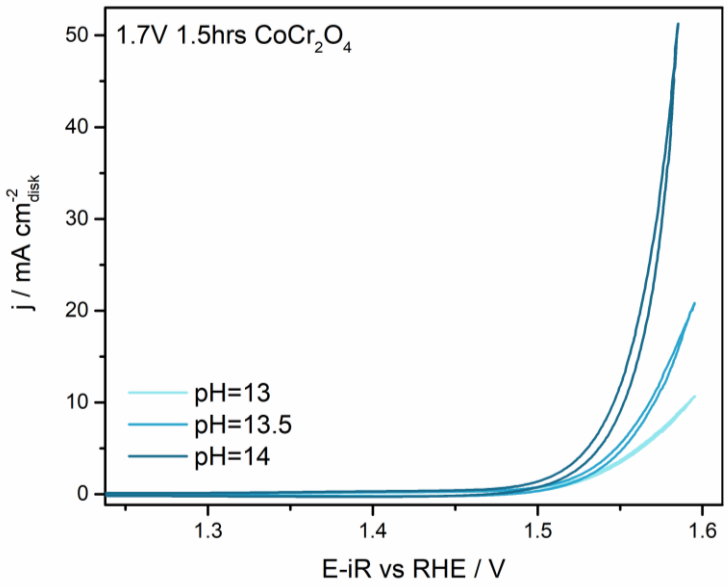

Figure S38. pH dependent OER activity for Act-$CoCr_2O_4$ after CA at 1.7V for 1.5 hours.

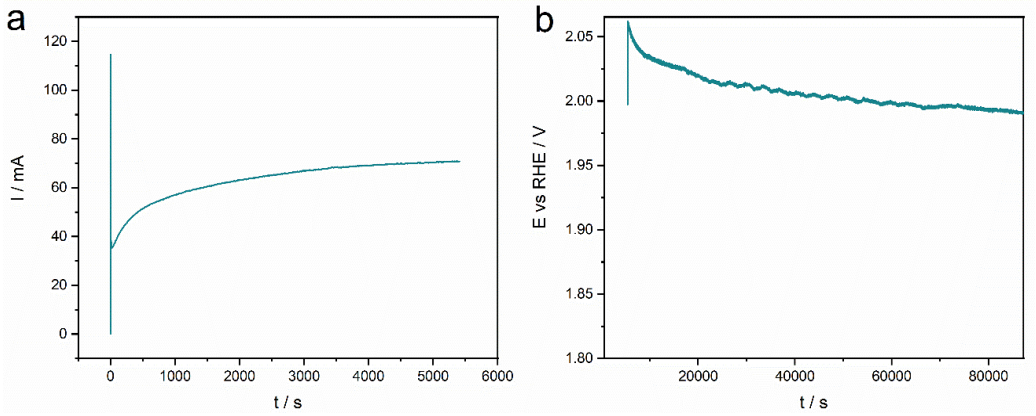

Figure S39. (a) CA test for $CoCr_2O_4$ loaded on carbon paper at 1.7V for 1.5 hours. (b) CP test for $CoCr_2O_4$ loaded on carbon paper for 24 hours under 100 mA cm^{-2}_{disk}. The catalyst is robust during the test. The good stability comes from the stable bulk structure of the catalyst. As indicated by XAS, XPS and TEM, only the surface Co reconstructs after the surface Cr leaches, while the bulk remains its spinel structure.

References

[1] L. Liardet, X. Hu, *ACS Catal* **2018**, *8*, 644–650.
[2] Y. Du, Y. Zhu, S. Xi, P. Yang, H. O. Moser, M. B. H. Breese, A. Borgna, *J Synchrotron Rad* **2015**, *22*, 839–843.
[3] B. Ravel, M. Newville, *J Synchrotron Rad* **2005**, *12*, 537–541.
[4] X. Yu, O. Wilhelmi, H. O. Moser, S. V. Vidyaraj, X. Gao, A. T. Wee, T. Nyunt, H. Qian, H. Zheng, *J Electron Spectrosc Relat Phenom* **2005**, *144*, 1031.
[5] J. Zhang, J. Fang, *J Am Chem Soc* **2009**, *131*, 18543–18547.
[6] T. L. Barr, S. Seal, *J Vac Sci Technol A* **1995**, *13*, 1239–1246.
[7] C. Wei, Z. Feng, G. G. Scherer, J. Barber, Y. Shao-Horn, Z. J. Xu, *Adv Mater* **2017**, *29*, 1606800.
[8] M. Görlin, J. Ferreira de Araújo, H. Schmies, D. Bernsmeier, S. Dresp, M. Gliech, Z. Jusys, P. Chernev, R. Kraehnert, H. Dau, P. Strasser, *J Am Chem Soc* **2017**, 139, 2070–2082.
[9] A. Grimaud, O. Diaz-Morales, B. Han, W. T. Hong, Y. L. Lee, L. Giordano, K. A. Stoerzinger, M. T. M. Koper, Y. Shao-Horn, *Nat Chem* **2017**, *9*, 457–465.
[10] L. Trotochaud, S. L. Young, J. K. Ranney, S. W. Boettcher, *J Am Chem Soc* **2014**, *136*, 6744–6753.
[11] D. Xu, M. B. Stevens, Y. Rui, G. DeLuca, S. W. Boettcher, E. Reichmanis, Y. Li, Q. Zhang, H. Wang, *Electrochimica Acta* **2018**, *265*, 10–18.
[12] Y. Duan, N. Dubouis, J. Huang, D. A. D. Corte, Z. J. Xu, A. Grimaud, *ACS Catal* **2020**, *10*, 4160–4170.
[13] C. Yang, O. Fontaine, J. M. Tarascon, A. Grimaud, *Angew Chem Int Ed* **2017**, *129*, 8778–8782.
[14] H. Dau, P. Liebisch, M. Haumann, *Analytical and Bioanalytical Chemistry* **2003**, *376*, 562–583.
[15] L. Trotochaud, J. K. Ranney, K. N. Williams, S. W. Boettcher, *J Am Chem Soc* **2012**, *134*, 17253–17261.
[16] L. Trotochaud, A. R. Head, S. Pletincx, O. Karslıoğlu, Y. Yu, A. Waldner, L. Kyhl, T. Hauffman, H. Terryn, B. Eichhorn, H. Bluhm, *J Phys Chem B* **2018**, *122*, 1000–1008.
[17] K. A. Stoerzinger, W. T. Hong, E. J. Crumlin, H. Bluhm, M. D. Biegalski, Y. Shao-Horn, *J Phys Chem C* **2014**, *118*, 19733–19741.
[18] K. A. Stoerzinger, X. Renshaw Wang, J. Hwang, R. R. Rao, W. T. Hong, C. M. Rouleau, D. Lee, Y. Yu, E. J. Crumlin, Y. Shao-Horn, *Top Catal* **2018**, *61*, 2161–2174.
[19] J. Yang, H. Liu, W. N. Martens, R. L. Frost, *J Phys Chem C* **2010**, *114*, 111–119.
[20] I. Abidat, C. Morais, C. Comminges, C. Canaff, J. Rousseau, N. Guignard, T. W. Napporn, A. Habrioux, K. B. Kokoh, *J Mater Chem A* **2017**, *5*, 7173–7183.
[21] A. K. Friedman, W. Shi, Y. Losovyj, A. R. Siedle, L. A. Baker, *J Electrochem Soc* **2018**, *165*, H733–H741.
[22] R. Michalski, *Pol J Environ Stud* **2004**, *13,* 73-78.
[23] S. I. Shupack, *Environ Health Perspect*, **1991**, *92*, 7-11.
[24] Y. Wang, A. P. Jia, M. F. Luo, J. Q. Lu, *Appl Catal B-Environ* **2015**, *165*, 477–486.
[25] E. Ünveren, E. Kemnitz, S. Hutton, A. Lippitz, W. E. S. Unger, *Surf Interface Anal* **2004**, *36*, 92–95.
[26] M. C. Biesinger, C. Brown, J. R. Mycroft, R. D. Davidson, N. S. McIntyre, *Surf Interface Anal* **2004**, *36*, 1550–1563.